ABSTRACT

Characterization and Lifetime Prediction of Roller and Journal Bearings
in Si and SiC Motor Drive Applications

Hellen W. Chen, M.S.E.C.E.

Mentor: Annette von Jouanne, Ph.D.

In the electrified propulsion system, a variable frequency drive (VFD) controls an electric motor. In many cases, this electric motor is an induction motor, which has been called the workhorse of industry. With semiconductor switching device advancements enabling higher power density inverter drives, mitigation techniques are being explored to remedy common issues that arise such as damaging bearing currents to ensure smooth implementation into motor drive systems. As higher power applications are enabled, the components within motors (including bearings) must have the capacity to handle the potential problems that arise from higher slew rates of advanced wide band gap (WBG) semiconductor switching devices in inverter drives. This thesis explores the behaviors of roller and journal bearings under electrical discharge conditions that are common in advanced motor drive applications, comparing the results with some known characteristics of ball bearings under similar conditions.

Characterization and Lifetime Prediction of Roller and Journal Bearings in Si and SiC Motor Drive Applications

by

Hellen W. Chen, B.S.

A Thesis

Approved by the Department of Electrical and Computer Engineering

Kwang Y. Lee, Ph.D., Chairperson

Submitted to the Graduate Faculty of
Baylor University in Partial Fulfillment of the
Requirements for the Degree
of

Master of Science in Electrical and Computer Engineering

Approved by the Thesis Committee

Annette von Jouanne, Ph.D., Chairperson

Emmanuel Agamloh, Ph.D.

Alex Yokochi, Ph.D.

Accepted by the Graduate School
May 2023

J. Larry Lyon, Ph.D., Dean

Page bearing signatures is kept on file in the Graduate School.

TABLE OF CONTENTS

LIST OF FIGURES

LIST OF TABLES

ACKNOWLEDGMENTS

First, I would like to give all glory to God our Father, who is the Provider of every good thing. I am grateful for my husband Paul and my family's endless support and prayers for my academic journey. Of course, none of this would be possible without the Baylor Graduate School and my advisors, Drs. von Jouanne, Yokochi, and Agamloh. Finally, I'd like to thank my colleagues from the BEARs lab for the immense help in completing this degree and constant encouragement and friendship inside and outside the research lab.

CHAPTER ONE

Introduction

As technology advancements allow for more electrification within the transportation sector, research continues to expand from electric vehicles and heavy-duty utility trucks to other ground transport such as rail and even into aircraft and ship applications. The goals for electrified transportation include enabling increased efficiency and energy savings, reduced emissions (especially when the electricity is being generated from renewable resources) and increased performance. To meet these efficient electrified propulsion and transportation goals, next generation electric motor drive technologies with very high power density are essential.

Background

Variable frequency drives (VFDs) are used in a variety of motor drive applications, including electrified transportation, due to their versatile functions and high efficiency operation compared to standard 60 Hz operation of motors using balanced AC power mains. Traditional VFD propulsion technologies use silicon (Si) based insulated-gate bipolar transistors (IGBTs) which are the power semiconductor switching devices used in power electronic inverters used to convert DC to AC to drive induction machines [1]. High power, wide bandgap (WBG) silicon carbide (SiC) power semiconductor switching devices enable much higher efficiencies and power densities and are thus a much-needed replacement for traditional silicon (Si) based power electronic devices in electric propulsion systems. The SiC WBG switches exhibit faster turn on/turn off times (slew rates) leading to less loss and higher efficiency. A challenge to advancing to SiC switches for higher performance propulsion drives is that the higher slew rates can result in damaging motor bearing currents [2], which can lead to electric discharge machining (EDM) and premature bearing failure. Thus, much research must be done to successfully implement WBG/SiC devices in motor drive systems to enable high performance motor drives for more efficient electrified transportation.

To complement higher power motors that run at high speeds, cylindrical roller bearings are often found in applications ranging from 300 to 1000's of horsepower [3]. Because roller bearings are designed for radial load capacity, they are typically found on one end (free end) of a belt-driven motor while the other end (fixed) has a ball or other type of bearing to handle both radial and axial load [3]. A different type of bearing that is used in even higher power applications (>10,000 hp) are journal bearings, which are often used in propulsion systems (e.g., in a full-electric ship) [3].

Literature Review

Formerly, motors were driven by AC power mains, but with the implementation of inverter drives, the signals are generated through pulse-width modulation (PWM) using switches. A common VFD topology for a three phase system includes a two-level, six-switch (TLSS) inverter, shown in Fig. 1.1 [1].

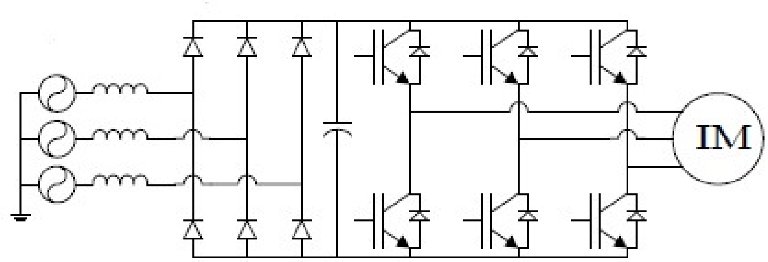

Figure 1.1. VFD topology with (left to right) three phase AC power inputs, diode bridge rectifier, and a TLSS PWM inverter driving a three phase induction motor [1].

However, the high frequency PWM phase voltages do not sum to zero, causing common mode voltage (CMV, shown in Fig. 1.2(a)) which leads to imbalance and often produces a voltage that rides on the shaft [1]-[3]. CMV can be calculated using Eq. (1.1):

$$V_{com} = \frac{V_{an}+V_{bn}+V_{cn}}{3} \tag{1.1}$$

where V_{com} is the common mode voltage, and V_{an}, V_{bn}, and V_{cn} are the phase voltages, while the nominal shaft voltage is ~1/25th of the CMV [1]. The relationship between CMV and shaft voltage is explained further in [1]-[3], including discussion on the bearing voltage ratio (BVR) theory [3], but the focus of this thesis is on mitigating EDM damage that results from parasitic currents that result from the many parasitic capacitances found in a motor under VFD operation (Fig. 1.2(b)). When the motor shaft voltage exceeds the dielectric (insulating) capability of the bearing, the voltage shoots through the bearing as a bearing current discharge [3], labeled i_{EDM} in Fig. 1.2(b). Note that this current most typically occurs on the drive end (DE) of the motor due to loading [5] because of the higher axial force when coupled to a load as opposed to the non-drive end (NDE) being uncoupled.

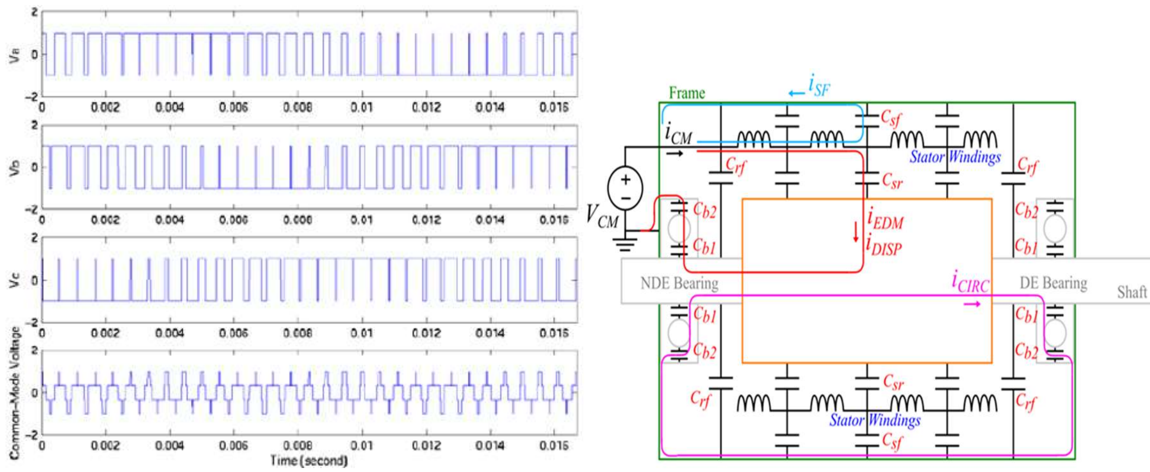

(a) (b)

Figure 1.2. (a) PWM inverter phase voltages, denoted by Va, Vb, Vc and the corresponding CMV [1] and (b) Current paths within a motor due to high frequency parasitics such as C_{b1} and C_{b2}, bearing capacitances; C_{sr}, stator-to-rotor capacitance; C_{rf} , rotor-to-frame capacitance; C_{sf}, stator-to-frame capacitance [3].

Rolling element bearings require grease to reduce friction, though the properties of the grease depend on several factors such as rotational speed, load, and temperature [6]. When an EDM current pulses through a bearing, the dielectric capacity of the grease is overcome, creating a path for the current to travel from the shaft to the inner race through the ball and into the outer race [2]. Depending on the film thickness of the lubricant and other properties of the system [6], the energy of the EDM bearing current discharge can heat the ball in the bearing through this path so much that it exceeds the steel's liquidus temperature of 1350 °C. The melted steel then sloshes around the bearing, causing damage which can be seen under a microscope [2] and therefore accelerates mechanical failure of the bearing.

Bearing damage detection. About 40% of electric motor failures are bearing related [7]. Monitoring the health of a bearing is therefore essential and can be achieved through multiple methods, but most used is bearing or machine vibration. Figure 1.3

shows the ISO standard used in industry to monitor bearing health using velocity vibration measurements, and more discussion and a demonstration of this method is found in [3].

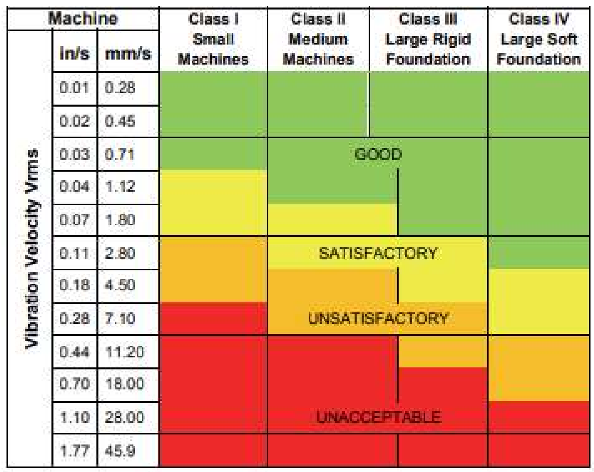

Figure 1.3. ISO 10816-1 Standard for Machine Vibration Measurements [8].

Other non-intrusive ways to monitor vibration include using acoustic emissions [9], accelerometers [10]-[11], piezoresistive devices or piezoelectric sensors (i.e., strain gauges [3], [12]) [13], or even ultrasound devices. With frequency spectrum analysis, damage can also be detected with bearing defect frequencies [3], [7], [12] or motor current signatures [1], [11], [14]. Ultrasound is an emerging method for monitoring lubrication health in machines [15], [16], but it has not yet been widely explored for vibration or bearing health analysis. Ultrasound instruments can sense signals in frequencies above 20 kHz to 100 kHz, beyond what the human ear can hear audibly [17]. Because of the shorter wavelengths of ultrasonic signals, subtle changes within a component can be detected at its source of friction before failure occurs [17].

The typical trend for bearing failure follows an exponential curve, where the damage within the bearing will slowly appear at first but will quickly accumulate after a certain threshold. The factors that accelerate rapid bearing deterioration include mechanical damage (via loading, extreme operating temperatures, and lubricant properties/behaviors) as well as electrical wear, such as EDM, that ultimately causes excessive friction and eventually leads to failure [12], [18].

Studying the damage within the bearing after failure has also been informative on bearing lifetime and damage behaviors. The morphological damage from energy discharges is further explained in [18], which lists several characterized damage types found on bearing races and rolling elements. Among these are frosting, pitting, fluting, spark tracks, and welding [18], which can appear as spots in the order of micrometers called pits and pillars. Electrical discharges can also affect the lubricant, which then exacerbates the damage on the solid components of the bearing [18]. Scanning electron microscopes (SEMs) have been used to image and measure the defects. A new technique explored in the lab [3], [12] uses a 3D laser scanning microscope (3DLM) which allows for similar functions to an SEM at greater magnifications. The main difference between these two microscopes is the SEM's ability to view the chemical composition of the sample, but for the purposes of this thesis, the 3DLM was used to retrieve higher resolution captures and roughness parameters calculated by the software.

There are several mitigation techniques for bearing currents, such as shaft grounding devices, insulated bearings (ceramic or coated), common-mode filters, dual bridge inverters, and conducting grease to name a few [1], [12], [19]. However, most of the mentioned methods can be costly, either in monetary terms or in maintenance/down times of the motor drive system when implemented. Using grease with higher electrical conductivity is a desirable method due to a lower cost than the other alternatives.

Increasing the conductivity of the grease within a bearing, as opposed to insulating the bearing components, creates new paths for discharges to travel within the grease and lowers the energy shoot-through, reducing the EDM damage in the bearing. Conductive grease has been shown effective through several studies including [12] and [19] and will be further discussed as a method for mitigating EDM in Chapter Two.

Higher power bearings. As mentioned in the introduction, roller bearings are used for larger, high-speed motors that need high radial load capacity as well as the ability to handle a motor shaft's thermal elongation/contraction [20]. Most roller bearing types, like cylindrical roller bearings, are used in belted applications due to the limited ability to handle only radial load, although some roller bearings can also handle small axial load due to tapered geometries [20]. Roller bearings are commonly found in gearboxes, blowers/fans, and even wind turbines [20], [21]. This thesis investigates small cylindrical roller bearings, specifically open roller bearings with a removable outer ring. Common roller bearing failures are due to oil lubricant breakdown or low load conditions, which can cause slippage between the rollers and raceways and result in smear or skid damage on the bearing surfaces [21], [22].

Journal bearings, also known as sliding or plain bearings, are sliding contact bearings composed of a housing and a journal (shaft) that spins within the housing [23]. These bearings are used in large industrial applications due to their robustness and ability to handle extreme load. The bearing is lubricated with oil instead of grease to form a thin layer of lubricant, separating the shaft from the housing and reducing friction between the two components. Lubrication is often replaced as the bearing is running, using drip lubrication, pressurized lubrication, and other methods [23]. There are both solid and split housing types depending on the application, and for this work, split housed journal bearings are used for easy access to the bearing liner/surfaces inside the housing. Like rolling element bearings, journal bearings can also experience oil lubricant breakdown that leads to bearing failures due to increased friction. Journal bearing life can also be affected by mechanical misalignments within the bearing housing, shaft imbalances, or even electrical excitation if used with electric motor systems, all of which can cause vibrations and wear [11], [24]. A typical type of wear found in journal bearings is babbitt fatigue which is caused from a variety of factors leading to cracks on the surface of the bearing housing [11], [25]. The author could not find any literature on EDM damage on journal bearings at this time.

Conclusions from Literature Review and Motivation for Research

In moving to WBG devices in VFDs and motor drive systems, the electrical damage within motors and specifically bearings must be mitigated to ensure a smooth transition to an electrified future. Furthermore, bearing data is essential in creating a standard for bearing aging such as vibration analysis, but many other techniques in classifying damage involve cutting the bearings open to inspect and image the balls and races using microscopes. Finding a non-intrusive way to collect data on what is happening inside the bearing enables a new way to monitor bearing health during discharges or accelerated bearing aging tests. While many have studied the effects of EDM within ball bearings, higher power bearings have yet to be investigated under these high electrical stress conditions. This thesis will explore the characteristics of EDM damage on cylindrical roller bearings and journal bearings using the methods described above and provide a comparison on the lifetime of each bearing compared to a ball bearing using accelerated aging experiments.

CHAPTER TWO

Preliminary Research

In this chapter, the preliminary comparison on EDM in motor bearings driven by Si and SiC inverters is investigated. The primary motors used were the 5 hp Toshiba 0054SDSR41A induction machines (IMs). Shaft voltages and bearing currents are analyzed under fully loaded and no load conditions. After categorizing the behavior of normal/stock grease, commercially available conductive greases were also tested.

Modified Induction Motor Research and Testing (with Loading)

Figure 2.1 shows a testbed on which experiments were performed on IMs, both modified and unmodified, for no load and fully loaded conditions and capabilities for exploring advancements with WBG devices. The Typhoon Hardware-in-the Loop (HIL) 402 is used as a system level controller to run the SiC inverter [4]. Because SiC devices are a new technology and costly, much of the work has focused on identifying and mitigating the problems that come with WBG devices while this work compares motor system efficiencies with widely used Si drives. The switching frequency for all modified motor tests was 10 kHz. Due to the exacerbated problem of bearing currents in SiC driven IMs, IMs were modified such that an insulating sleeve was installed on the bearing housing, with a section of the housing cut so a jumper wire could be soldered directly on the bearing outer race and grounded to the motor frame [26]. With a new path for EDM currents to travel, the bearing currents were monitored on an oscilloscope using a current probe, while the shaft voltages were also shown via a voltage probe connected to a shaft brush that was fixed on the motor housing (Fig. 2.1). Adding a wire to the modified motor causes new parasitic capacitances, which is further discussed in [3]. For the purposes of this preliminary work, the bearing currents are analyzed as captured from the oscilloscope, and further details of the no load vs. loaded experiments are discussed in the later sections of this chapter. Note the power density increase, where the Toshiba Si drive is 7 kW, while the Cree SiC inverter is 250 kW.

Figure 2.1. Testbed to vary load, temperature, and speed of IMs [3].

To begin the comparison between the two drives and their corresponding bearing discharge characteristics, no load (uncoupled) tests using the Si then the SiC drive were performed on the modified motor with stock 6306 shielded deep groove ball bearings. The insulating sleeves were on both the DE and NDE, and only the DE bearing currents were captured. CMV data (using methods in [3] and [12]) and shaft voltage data on the DE were also taken. Fully loaded tests were then performed using an ABB ACS800-U11-0020-5 drive and its corresponding DriveWindow 2.40 software via torque control on a

Marathon VVB184THTS8028ESL IM. The load was applied after steady state conditions were reached in the motoring IM (shown as the left IM of the loaded testbed of Fig. 2.1, driven by the Si VFD or SiC inverter). Figure 2.2 shows the shaft voltages and bearing currents of Si and SiC tests under no load (left) and fully loaded (right) conditions for a stock 6306 bearing. The Si tests resulted in higher maximum bearing currents in no load conditions, agreeing with the literature which reveals that no load conditions tend to increase the severity of bearing damage and therefore see an increase in bearing currents [3], [5], [12]. Comparing between the two drives, the SiC inverter causes much higher bearing currents than the Si VFD, which was expected due to the SiC switches' WBG characteristics. However, at the timescale of 1 ms, it is hard to see a noticeable decrease in the bearing current of the loaded SiC test compared to the unloaded one.

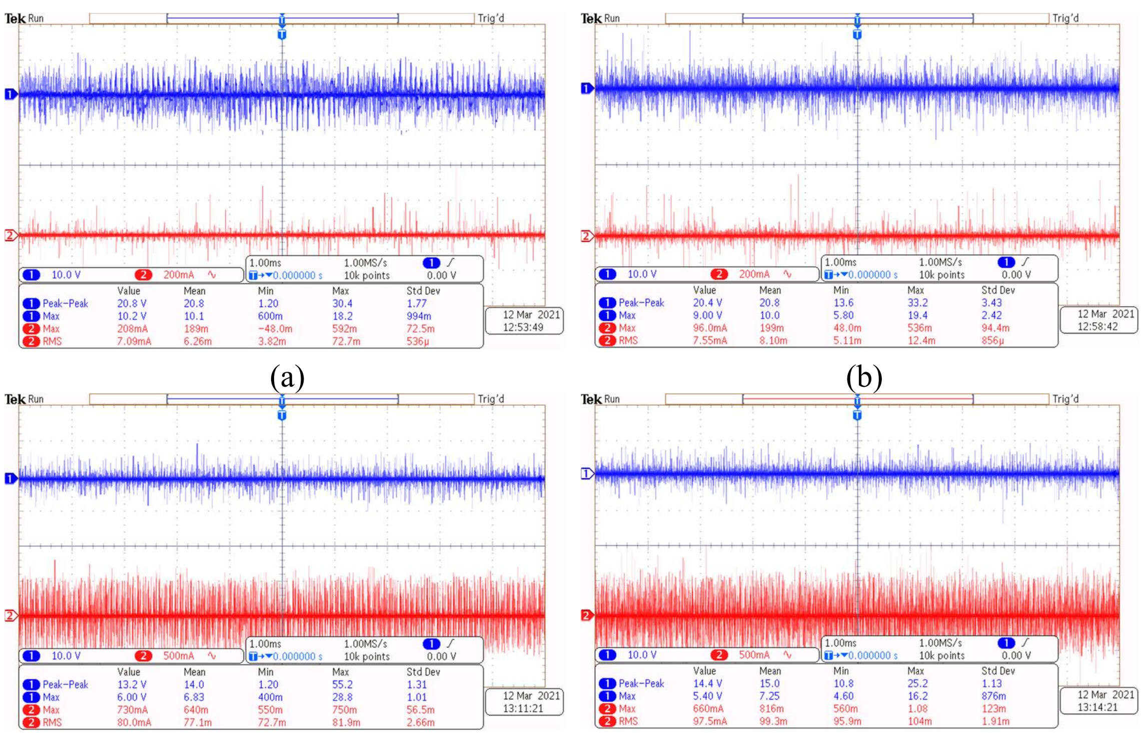

(a) (b)

(c) (d)

Figure 2.2. Shaft Voltage (blue) and Bearing Current (red) for (a) unloaded Si test, (b) fully loaded Si test, (c) unloaded SiC test, and (d) fully loaded SiC test. Note: The

bearing current scale for Si tests was set to 200mA/div while the SiC scale was 500mA/div due to higher bearing current characteristics.

Figure 2.3 uses a smaller time scale of 1 µs to zoom into the energy discharge pulse for the SiC tests. Note that the bottom part of the unloaded bearing current is covered by the displayed measurements in Fig. 2.3(a), but the peak-to-peak measurement clearly shows that the unloaded bearing current was higher than the loaded bearing current (2.30 A vs. 1.88 A, respectively). These SiC results again confirm the findings from literature that unloaded conditions experience higher bearing currents than loaded conditions for electric motors driven by switches.

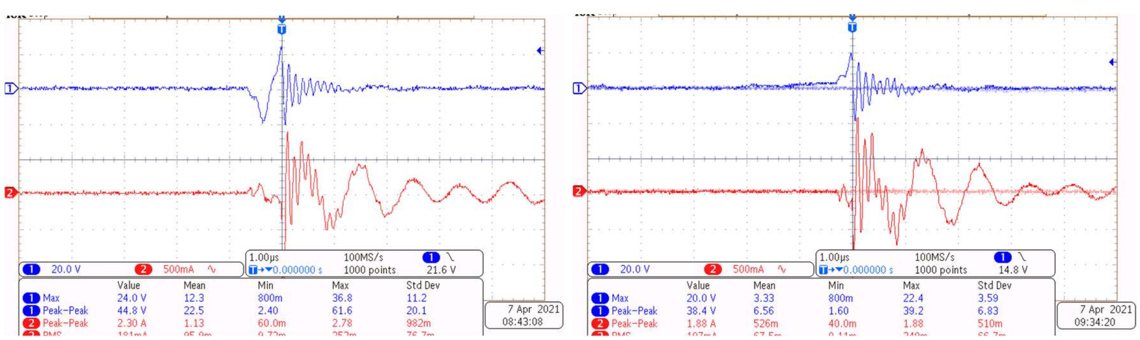

(a) (b)

Figure 2.3. SiC Test Shaft Voltage (blue) and Bearing Current (red) for (a) Unloaded Conditions, and (b) Fully Loaded Conditions.

The Si and SiC tests for unloaded and loaded conditions should be repeated to gather more consistent data across different time scales, longer sample record lengths, or even under partially loaded conditions. It may be beneficial to capture the no load shaft voltages and bearing currents after a machine had been loaded, since the tests were conducted where no load data was first collected before loading the motor for full load data. Nevertheless, these preliminary results confirm that in both Si and SiC driven motors, the bearing currents are higher in unloaded conditions.

It has been found that phase currents could also indicate a number of component failures within a motor drive system in the frequency domain via sidebands to the fundamental frequency [1], [11], [13]. This spectrum analysis was compared using loaded tests run by the Si VFD between an undamaged and an EDM damaged bearing on the modified motor. The results yielded no noticeable changed between the two FFTs, and this method needs further investigation to be applied to detect EDM damage in bearings.

Conductive Grease Research and Testing (with Loading)

The lab conducted a survey of unloaded and loaded experiments, replacing stock grease with a variety of commercially available conductive greases. These greases were selected based on viscosity, resistivity, and operating temperature range to compare with conventional greases. A method was developed to clean rubber sealed (as opposed to metal shielded) 6306 ball bearings with paint thinner, then repacking them with conductive grease to the industry standard (1/3 full) and replacing the seals. Each bearing was spun on the motor to reach steady state conditions for the lubricating film to form before measurements were taken. The fully loaded IM test results are shown in Table 2.1. The greases are listed under a code name for confidentiality purposes since the greases used came from a couple different manufacturers.

Table 2.1. Fully loaded test results conducted with Si and SiC inverter drives.

Grease	Viscosity [mm/s]	Resistivity [Ω*cm]	Avg Max Shaft Voltage Si	Avg Pk-Pk Bearing Current Si	Avg Max Shaft Voltage SiC	Avg Pk-Pk Bearing Current SiC
X	-	23	11.6 V	33.04 mA	23.7 V	1.44 A
Y	~127	160	3.73 V	59.3 mA	9.9 V	2.45 A
Z	36	623	1.7 V	274 mA	7.3 V	1.58 A
Conven-tional	96	$1*10^7$	18.9 V	458.4 mA	19.3 V	1.73 A

A clear distinction exists between the conductive greases' (X, Y, and Z) results and the shaft voltages and bearing currents of the conventional grease for both the Si and SiC tests. X performed the worst in both tests compared to Y and Z, due to its typical application designed for non-moving parts. The results for Y showed lower bearing currents for the Si driven test, yet in the SiC test, it yielded both higher voltages and currents than Z. Nevertheless, all the tested conductive greases lowered the shaft voltage and bearing current values from the stock greases in a manufactured bearing. However, these shaft voltages and bearing currents did not reach below the discharge energy threshold of 17 nJ for EDM damage [26].

To take the concept of electrical conductivity further and to try to lower the discharge energies to where no damage could result from the overshoot, carbon nanoparticles were integrated into the Y and Z. Each grease was mixed with 10% carbon nanoparticles by mass, packed into bearings that went on both ends of the motor, and retested using the SiC drive under the fully loaded condition. However, upon testing Z with the integrated nanoparticles, the shaft voltages were higher by an average of 3.8 V while the bearing currents were about the same as the previous test of Z without nanoparticles. The Y mixture with nanoparticles (Y10) yielded much lower results than by itself or even the results of Z in the SiC test in Table 2.1, averaging 2.59 V for the maximum shaft voltage and 0.58 A for the peak-to-peak bearing current. Screen captures of the shaft voltage and bearing current of conventional grease vs. Y10 under full load testing are displayed in Fig. 2.4.

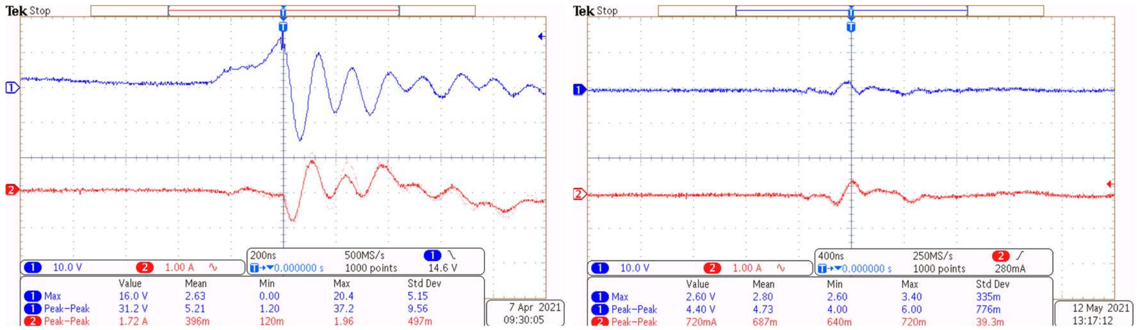

(a) (b)

Figure 2.4. SiC Fully Loaded Test Shaft Voltage (blue) and Bearing Current (red) for (a) Conventional Grease, and (b) Y10.

The comparison above shows the drastic improvement with Y10, revealing promise for the integration of conductive nanoparticles as a viable solution in mitigating damaging energy discharges that plague VFD motor systems. [12] builds on this idea of creating inverter duty bearings using a lab-created conductive grease mixture.

Lifetime Prediction Motor Experiment

A long-term test was run for about 74 days to test a hypothesis on bearing lifetime presented in [3]. The experiment was performed with an unloaded 5 hp Toshiba motor driven by the SiC inverter, in which a normal (stock) C&U 6306Z ball bearing at the DE of the motor was predicted to fail after 60±8 days of continuous operation [3]. The switching frequency of the SiC inverter was set to 50 kHz, and the NDE bearing was insulated with Delrin so that all the EDM caused by the SiC inverter would be forced through the DE test bearing. It was predicted that the bearing failure could be indicated by a velocity vibration measurement of about 7 mm/s, taken by a Fluke 805 FC meter [3]. The motor was run continuously for about 70 days when an audible rhythmic “crunching” noise was heard to indicate bearing failure. The vibration measurements are shown in Fig. 2.5, where the blue stars indicate data points taken throughout the experiment's duration.

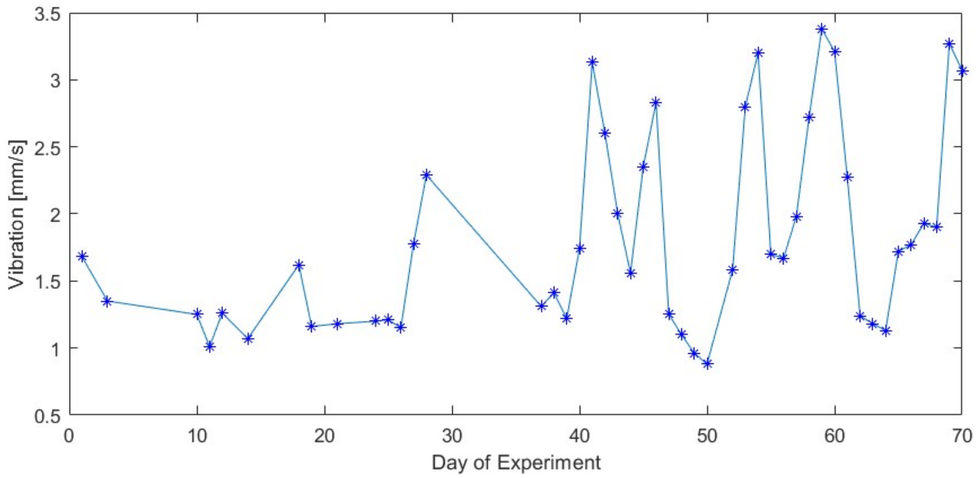

Figure 2.5. Vibration Measurements on DE Bearing for Lifetime Prediction Test.

As seen in the figure, there is a slight increase overall, but no consistent pattern shown in the vibration measurements. The threshold of 7 mm/s was never reached, likely due to the no load condition that may have contributed to inconsistent motor behavior. Because no real pattern had formed after 40 days of using only the Fluke meter to monitor the bearing vibrations, other measurements were implemented, including audio and strain using the shielded piezoelectric sensor (TE Connectivity 1-1000288). The audio (measured with a simple sound level meter/microphone) showed an increase of 6 dB between day 40 and day 70. Figure 2.6 shows the fast Fourier transform waveforms from the piezo measurements that were taken, comparing the first data set to one taken when the bearing failed. A slight increase in amplitude is seen in the FFT, especially in the high frequencies, but nothing drastic to indicate bearing failure. Although the piezoelectric sensor was shielded, there was much noise present in both the time and frequency domain of the signals, due to the electromagnetic interference (EMI) of the SiC inverter drive system [4]. If this method is further researched and advanced to find which frequencies reveal certain characteristics of vibration, piezoelectric sensors could be used to measure damage in bearing aging for many applications.

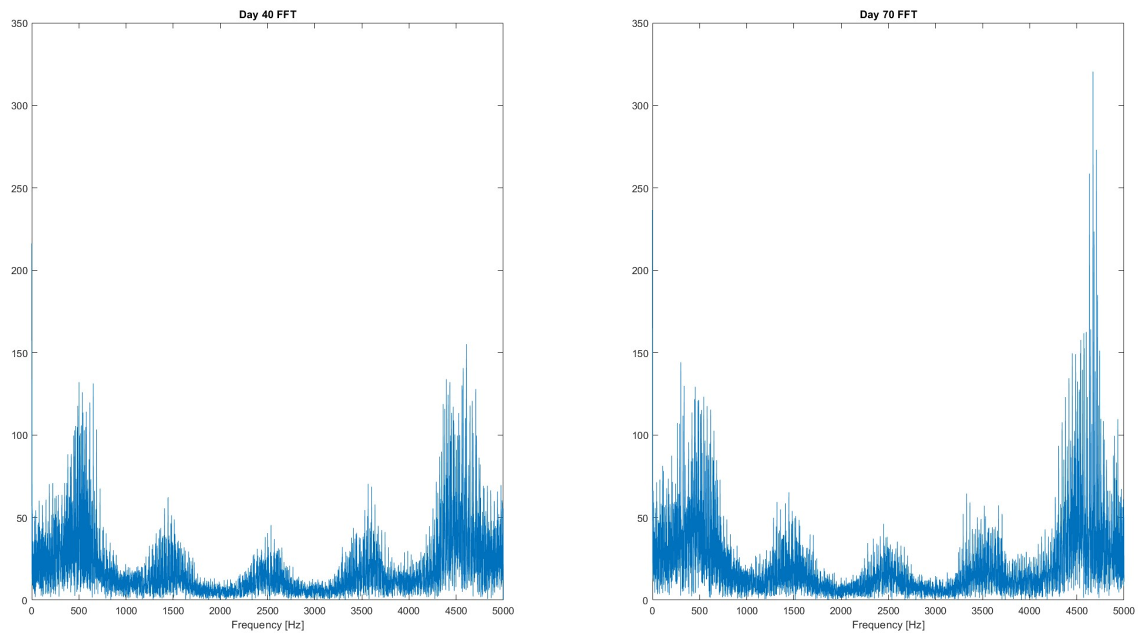

Figure 2.6. Piezoelectric FFTs from DE Bearing for Lifetime Prediction Test.

The phase current FFTs were also taken after the bearing failed, and as in previous work, the sidebands did not appear to indicate bearing failure. To confirm this, new bearings were also put on the motor, and the phase current FFTs after bearing replacement were the same as the failed bearing. Therefore, the frequency spectrum analysis of phase currents cannot be applied for EDM damage in bearings without further research.

Another experiment that explored the use of the Fluke meter, piezoelectric sensor, and current spectral analysis was performed on an unmodified IM. The SiC inverter driven tests were run under no load conditions, comparing the vibrations of a normal bearing with stock grease and a bearing packed with the Y mixture mentioned in the previous section. These longer term tests yielded similar results to those of the lifetime prediction motor experiment, confirming the piezoelectric sensor was prone to EMI and noise, the Fluke meter measurements were not always consistent in detecting failure, and no change in the current FFT sidebands between damaged and undamaged bearings for either the normal grease or conductive grease mixture. In conclusion, EDM should be monitored via other non-intrusive methods, which will be explored in later chapters.

CHAPTER THREE

Testbed Development and Data Collection Methods

To study the effects of EDM on higher power bearings like cylindrical roller bearings and journal bearings, testbeds similar to the bearing testbed of [3] was created. This type of accelerated aging experiment via precise control of EDM discharge energies enabled the study of electrical wear while minimizing the effects of mechanical loading or other imbalances that result from a machine/motor testbed. More discussion on the parasitic components is found in [3], and the electrical energy discharge control software and hardware are explained further in [3] and [12]. Note that temperature control was not applied to these tests. This chapter will mainly focus on the mechanical design of the bearing testbeds as well as data collection methods for each testbed.

Lifetime Prediction of Roller Bearing using Accelerated Aging on Belted Testbed

Figure 3.1 shows the belted testbed that was developed for cylindrical roller bearings under accelerated aging with EDM discharge control. Because roller bearings can only handle radial load, a v-belt pulley system was used to couple a 5 hp rotor to a 1 hp Toshiba motor, which was driven by a 15 kW Toshiba VFD at the rated speed of 1800 RPM. The rotor was taken from the 5 hp Toshiba IMs used in the preliminary research of Chapter Two, which was used so that loading characteristics would be similar to tests that have already been done in studying EDM effects [3], [5]. N-type (removable outer race) FAG N306ETVP2 roller bearings were used so that a comparison could be made with the 6306 ball bearings that were also tested under the same degradation method [3], where both types had 30 mm (bore diameter) x 72 mm (outer diameter) x 19 mm (width) dimensions. WD-40 3-IN-ONE Multi-Purpose Oil was used for relubrication when needed, because the cylindrical roller bearings were open bearings as opposed to sealed or shielded. The rotor was fixed using a ball bearing on the NDE because ball bearings can handle both radial and axial load. The discharges were applied to the 5 hp rotor through a shaft brush at a rate of ~25 kHz as in [3] and were monitored using an oscilloscope.

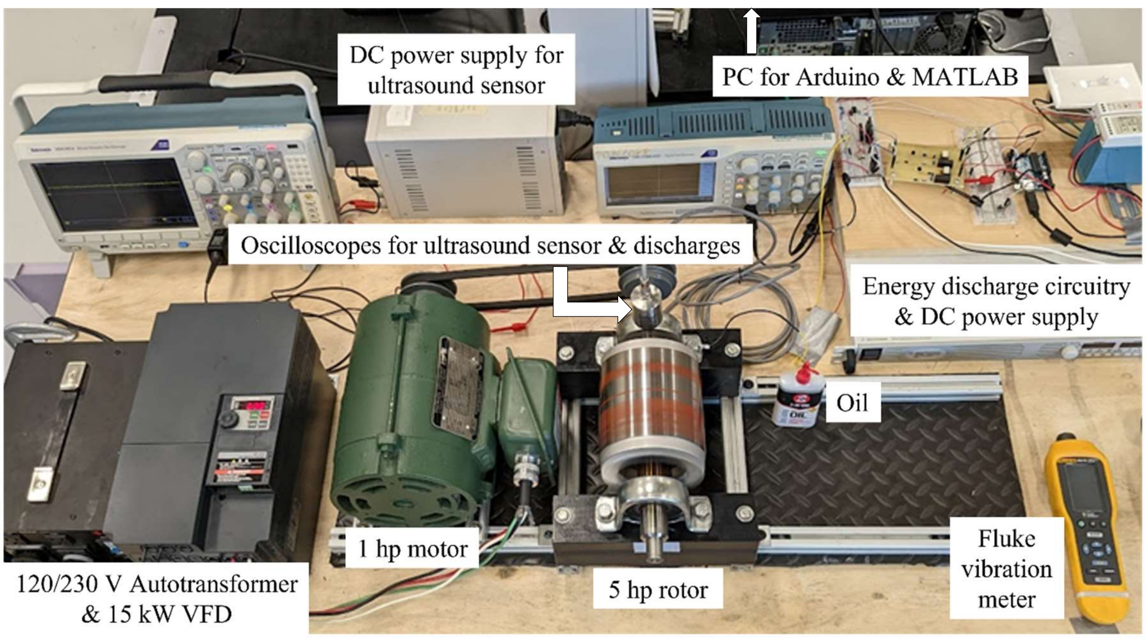

Figure 3.1. Belted Testbed for precise control of EDM discharges.

By nature of the belt and pulley system, the energy discharges were isolated to the rotor, just as the coupled testbed of [3] had isolated the discharges using an insulated coupling. It is important to note that an SKF 6306-2Z/C3GJN ball bearing was used on the NDE for most of the experiments (bottom side of rotor), but to study the effects of the EDM discharges further, a hybrid ceramic bearing (MR6 306 C-HIP-VV/C3) replaced the steel ball bearing so that the NDE would be insulated, causing the energy discharges to only go through the DE (pulley side of rotor). Before running tests, the discharge characteristics and energies were confirmed to be the same as those presented in [3] because the same equipment, wires, and circuit components were used, despite the different coupling method. Methods from [27] were used to ensure proper installation and maintenance of the v-belt pulley system throughout the experiments.

Data Collection Methods for Belted Testbed

The Fluke 805 FC meter was used to measure the velocity vibration measurements of the DE while also monitoring the NDE to ensure that the system was aligned throughout the experiments. The Fluke measurements were taken from the sides of the bearing pillow blocks, taking the average of 3 readings at a time. The temperatures of both the DE and NDE were consistently 26 °C for all tests, which was also measured with the Fluke meter. An ultrasound sensor was introduced during the last two tests (it had not arrived earlier due to supply chain constraints). The UltraTrak 850S Smart Analog Sensor was selected for monitoring the roller bearing due to its ease of implementation and advertised application to bearings [17]. Table 3.1 shows how to analyze the ultrasound measurements according to NASA standards [17]. The sensor itself was mounted directly on top of the DE bearing pillow block, and a 200 Ω resistor was placed between the sensing output and ground wires so that a voltage probe fed the signal into an oscilloscope that was connected to the PC. An automated MATLAB script collected and saved the raw voltage data from the ultrasound sensor into a spreadsheet with timestamps, which was modified from the script created for piezoelectric sensor data in [3] (see the Appendix). The script also applied the transfer function of the UltraTrak

850S to the data and plotted the resulting dB measurement. Note that due to the slow update time of the sensor, acquiring 1000 data points took ~7 minutes, so the samples were not collected exactly at each 6 hour interval.

Table 3.1. Levels of change for ultrasound signals [17].

Alarm Indication	dB Value
Alarm 1: Requires Lubrication	Baseline + 8 dB
Alarm 2: Early Onset of Bearing Failure	Baseline + 16 dB
Alarm 3: Catastrophic Bearing Failure	Baseline + 35 dB

After the cylindrical roller bearings were tested, they were cleaned and cut open with a Taurus diamond ring saw for inspection under the 3DLM (OLYMPUS LEXT OLS5100) and analyzed using the OLYMPUS LEXT microscope software. Table 3.2 shows the magnification lens, zoom, and sample image area associated with each setting used. The "Super High Resolution" function was used for all image samples. The microscope automatically acquired three types of images: color, intensity, and height. The results presented in the following chapter show either the color or intensity image, depending on the resolution of the image setting, where the increased 4X zoom often made color images blurry, or if distracting colors from rust or other defects were present. All height images were corrected with the "auto" function on the software, which reduced noise and normalized curves on the surface of the sample, allowing for comparisons between images and defect size analysis. Two surface roughness measurements, R_a and R_q, were calculated by the software using the profile method (where lines were drawn perpendicular to the direction of the polish lines of the samples). Tilt removal was applied to all the line profile data. The arithmetic mean deviation (R_a) takes the "mean of the average height difference for the average surface" while the root mean square deviation (R_q) “corresponds to the standard deviation of the height distribution” [28]. Because the bearing cutting process caused the samples to be prone to scratches or rust, these two parameters were selected due to their stable nature and ability to not be “significantly influenced by scratches, contamination, and measurement noise” [28]. To compare between image samples, the surface roughness coefficient R_a/R_q was calculated, where a value closer to 1 reveals a higher surface roughness. Defect size parameters, such as diameter and height/depth of a pit or pillar, were also obtained using the analysis software.

Table 3.2. 3DLM Settings and Sample Areas.

Magnification Lens	Zoom Setting	Associated Sample Area
5X	1X	2569 µm x 2569 µm
50X	1X	259 µm x 259 µm
50X	4X	64.8 µm x 64.8 µm

Journal Bearing Comparison using Coupled DC Motor Testbed

A preliminary journal bearing testbed was set up and run for a few days for a mechanical test (Fig. 3.2). An Ametek Pittman Lo-Cog 14203S010 12 V DC Motor spun the ½” diameter shaft of the journal bearing using an insulated spider coupler. A split housing journal bearing was chosen due to easy access to the bearing wall so that image results could be taken with the 3DLM. A drip lubrication device was used to control the rate of the oil that was dispensed into the journal bearing from the top. The NDE of the journal bearing shaft was left unloaded to eliminate variables in vibrations and misalignments. A fan was used to keep the motor and bearing cool and avoid burning out the dc motor. Although it was found that proximity probes are commonly used to monitor the condition of journal bearings [11], no probes were found to be suitable for the size of journal bearings used for these experiments. The vibration velocity measurements and temperature measurements were taken with the Fluke meter as in previous bearing testbed procedures.

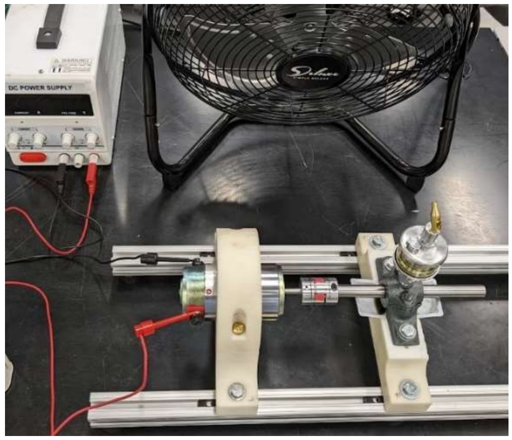

Figure 3.2. Preliminary Journal Bearing Testbed for Mechanical Investigation Only.

From the preliminary testbed, an accelerated aging testbed was built to investigate EDM damage on journal bearings. Figure 3.3 shows the testbed that includes the same energy discharge circuit that was used in the belted roller bearing testbed as well as in the bearing testbeds of [3] and [12]. These discharges were applied to the uncoupled shaft end of the journal bearing using a shaft brush and were monitored using a voltage probe connected to an oscilloscope.

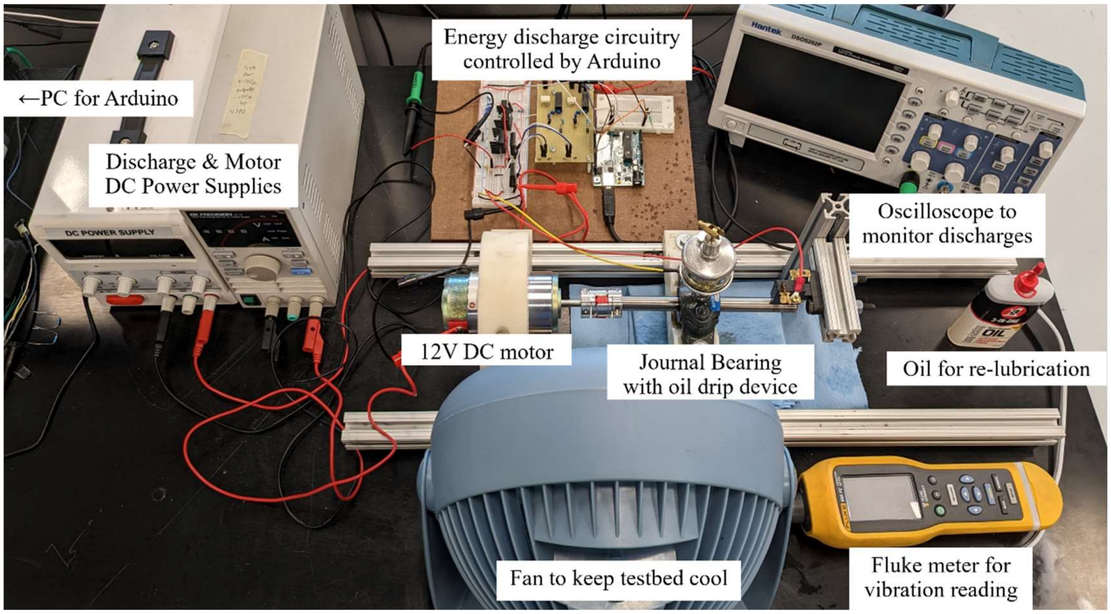

Figure 3.3. Journal Bearing Discharge Testbed.

Because the testbed was much smaller than the ball or roller bearing testbeds and the bearing itself had no clear area to mount additional sensors, only the Fluke meter was used to monitor the vibrations of the bearing. The tip of the meter was pressed against a groove on the bottom housing part because it was fixed and easily accessible. The journal bearings were also imaged using the 3DLM after testing using the same methods as described for the cylindrical roller bearing samples.

CHAPTER FOUR

Results and Discussion

Roller Bearing Results (Vibration & Nonintrusive Measurements, Imaging)

Table 4.1 shows the cylindrical roller bearing experiments that were conducted on the belted testbed. The new roller bearing (experiment no. 1) was not used on the testbed and was cut and imaged for comparison. For experiments 2–6, an SKF 6306-2Z/C3GJN ball bearing was used on the NDE. Note that the UltraTrak 850S sensor was used for experiments 7 and 8. The mechanical test (no. 2) was run for a week without any energy discharges occurring and was cut and imaged for comparison as well. A preliminary 5.5 V test (no. 3) correlates with the 5.5 V (nominal shaft voltage) test conducted on ball bearings in [3]. The parameters were the same (220 mA, 34 nJ) because the same energy discharge circuit and capacitors were used, and the 5.5 V roller bearing test was run continuously and stopped at 6.125 billion discharges (compared to 6.124 billion for the 5.5 V ball bearing test [3]). The rest of the experiments (4-8) were accelerated aging tests, also having the same parameters (4.12 A, 8100 nJ) as those conducted in [3]. The difference in number of discharge (and test duration) will be further discussed as results are presented for each experiment throughout this chapter.

Table 4.1. Cylindrical Roller Bearing Experiments.

Experiment No.	Discharge Voltage [V]	Energy/Discharge [nJ]	Number of Discharges	Test duration [days]	Notes
1	-	-	-	-	New, never spun bearing
2	0	0	0	7	Mechanical comparison
3	5.5	34	6,125,000,000	~4	Nominal shaft voltage, no significant damage
4	90	8100	~40,876,000,000	26	Not failed, minimal damage along “rollway” of the rollers, ~6 days where discharges slowed due to lack of oil
5	90	8100	10,260,000,000	5	Failed mechanically due to lack of oil and misalignments in testbed
6	90	8100	~100,610,000,000	57	Failed (audible) with visible fluting on outer race SKF bearing on NDE also failed, which experienced discharges that traveled down the shaft
7	90	8100	~50,094,000,000	31	Failed (audible) Ultrasound also indicated failure at ~40 billion discharges Visible fluting on all components (races & rollers) Ceramic bearing on NDE
8	90	8100	105,816,000,000	58	Not failed (only slight audible increase, no ultrasound failure) Light fluting on outer race Ceramic bearing on NDE

Note: The approximated number of discharges were due to unplanned lab power outages that shut off equipment.

Fluke Vibration Measurements

Surprisingly, the velocity vibration measurements taken with the Fluke meter revealed no change for all experiments run on the belted testbed. The first and last measurements of the mechanical test were 1.63 mm/s and 1.51 mm/s, respectively, revealing no change in vibration. For the 5.5 V roller bearing test, the vibration measurements were 1.79 mm/s at the beginning and 2.31 mm/s at the end of the test, also showing no change. Note that these measurements were almost identical to that of the 5.5 V ball bearing test. It was expected that the 90 V tests would follow the increase of vibration in the ball bearing tests, where all the tests were run to failure indicated by a measurement value of ~7 mm/s [3]. However, all the 90 V roller bearing tests had a range of 1.18–2.38 mm/s and 1.13–2.42 mm/s for the start and end Fluke measurements, respectively. Undoubtedly, there were some uncertainties in the values due to the sensitivity of the instrument used and the bearing pillow block being pressed by the sensor tip of the Fluke meter. Nevertheless, the unchanging nature of the vibration measurements is largely due to the v-belt pulley system of the testbed, which is more forgiving of misalignments than direct coupling by nature and therefore dampened the vibration of the overall testbed [10], [29]. Therefore, the vibration measurements were not helpful in monitoring the health of the roller bearings in these experiments using the belted testbed.

Experimental Results

Figure 4.1(a) shows a sample cut from the outer race of a new, never spun cylindrical roller bearing, with (b) and (c) showing the images taken from the sample under the 3DLM. All roller bearing samples were cut to 7-12 mm widths so that the race surface would be flat and easily imaged with the microscope. The larger, visible defects in Fig. 4.1(a) are water marks and other scratches from the bearing cutting process. The new bearing samples were only inspected for the roughness coefficients to compare with the bearings under test, since there were no defects to be found, as expected from a bearing that had never been spun apart from the manufacturing process.

(a) (b) (c)

Figure 4.1. New Cylindrical Roller Bearing Outer Race (a) cut sample and imaged at (b) 5X Lens, 1X Zoom and (c) 50X Lens, 1X Zoom.

Table 4.2 summarizes the average roughness coefficients from the roller bearing experiments. The measurement lines were drawn across areas of wear and fluting if applicable, since the “rollways” contribute the most to bearing failure due to contact of the bearing elements. Experiment 5 was excluded from the results because it failed due to mechanical reasons. Interestingly, there were no distinct patterns between the experiments. Though it was expected that the roughness would decrease as the samples decreased in image size due to increased resolutions, only experiment 8 followed the decreasing roughness coefficient pattern as the magnification and zoom increased. The roughness coefficients of experiments 1, 3, and 6 displayed the opposite behavior and increased as the resolutions increased. For experiment 1, the increasing coefficient could be due to the race being from a new bearing, so a higher resolution could have caused the microscope to capture more manufactured defects. Experiments 3-8 all experienced electrical discharges, but only 3 and 6 exhibited the increasing roughness coefficient pattern as magnification increased. The inconsistency between the roughness coefficient behavior was likely due to the images being taken at different locations between samples of different experiments. Therefore, for future experiments, samples from the bearings should be cut at the same locations, and the images should also be taken at the same spots so that comparable surface roughness measurements can be made. Of course, due to inconsistencies in the manufacturing process or testbed set up from bearing to bearing, there will always be errors in the measurements between experiments.

Table 4.2. Summary of Average Roughness Coefficients for Roller Bearing Experiments.

Experiment No.	Average Overall	Average for 5X Lens, 1X Zoom	Average for 50X Lens, 1X Zoom	Average for 50X Lens, 4X Zoom
1	0.7362	0.7202	0.7437	0.7929
2	0.7197	0.7563	0.6947	0.7055
3	0.7618	0.74131	0.7662	0.8067
4	0.7387	0.7411	0.7223	0.7567
6	0.7814	0.7620	0.7885	0.7991
7	0.7238	0.7541	0.7013	0.7459
8	0.7340	0.7709	0.7206	0.7162

For the 0 V mechanical test (experiment no. 2), it was decided that running the experiment for a week would be sufficient for the comparison of the defect sizes between the electrical energy discharge experiments. Figure 4.2 shows the images taken on the outer race from the bearing of the mechanical experiment. Fig. 4.2(c) was taken at the boundary edge of the rollers spinning. The defects from this image were 0.62 to 1.096

μm in diameter with heights of 0.388 to 0.71 μm. Compared to the new roller bearing, the bearing from the mechanical test has clear defects, easily seen under the 50X magnification lens.

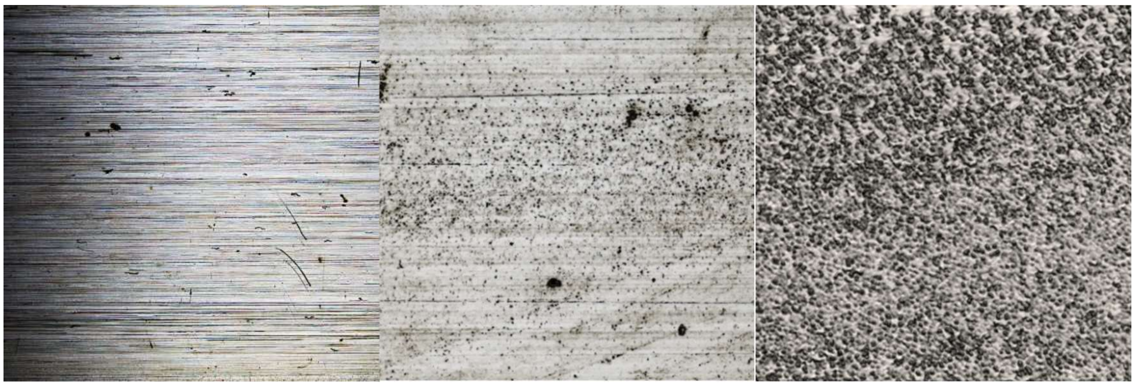

(a) (b) (c)

Figure 4.2. Experiment 2: Mechanical Roller Bearing Outer Race at (a) 5X Lens, 1X Zoom, (b) 50X Lens, 1X Zoom, and (c) 50X Lens, 4X Zoom.

Figure 4.3 shows images from the 5.5 V experiment. With the introduction of electrical discharges, the polish lines on the outer race of the 5.5 V test are visibly worn compared to the mechanical test, despite the shorter duration of the 5.5 V test. The energy discharges applied, though low in energy, caused the melting and cooling of the steel on the outer race. Recall that it was found that 17 nJ is the threshold for EDM damage [20], so with 5.5 V, 34 nJ discharges being greater than 17 nJ, EDM defects are present in the bearing. The darker spots on Fig. 4.3(a) are indicative of EDM, and as the images zoom in, the spots become more apparent, shown in both Fig. 4.3(b) and (c). In the higher magnification images (50X lens, 4X zoom), the pit/pillar diameters ranged between 0.571 μm to 1.186 μm. The correlated depths and heights of the defects ranged from 0.976 μm to 1.825 μm. The defect size parameters were clearly larger than those found on the mechanical test roller bearing. It is also important to note going forward that while some roller bearing images contain defects that look deeper, the defects in the height view were not deeper than the area surrounding them (Fig. 4.4).

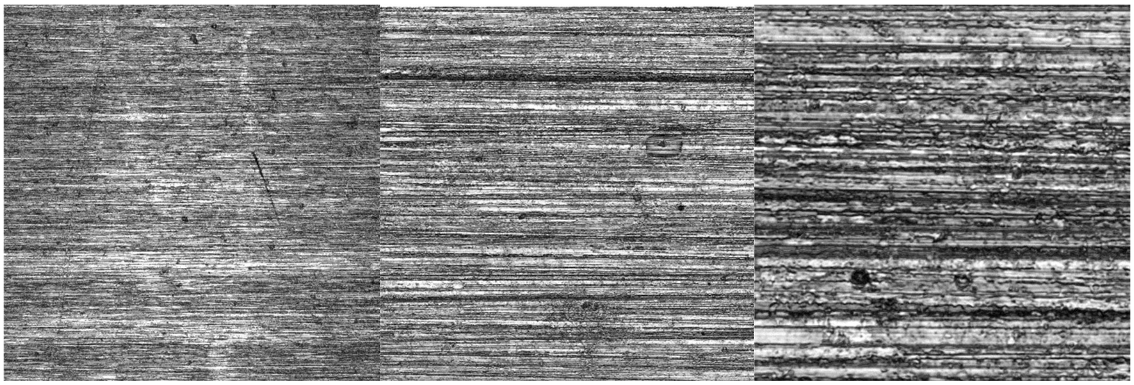

(a) (b) (c)

Figure 4.3. Experiment 3: 5.5 V Roller Bearing Outer Race at (a) 5X Lens, 1X Zoom, (b) 50X Lens, 1X Zoom, and (c) 50X Lens, 4X Zoom.

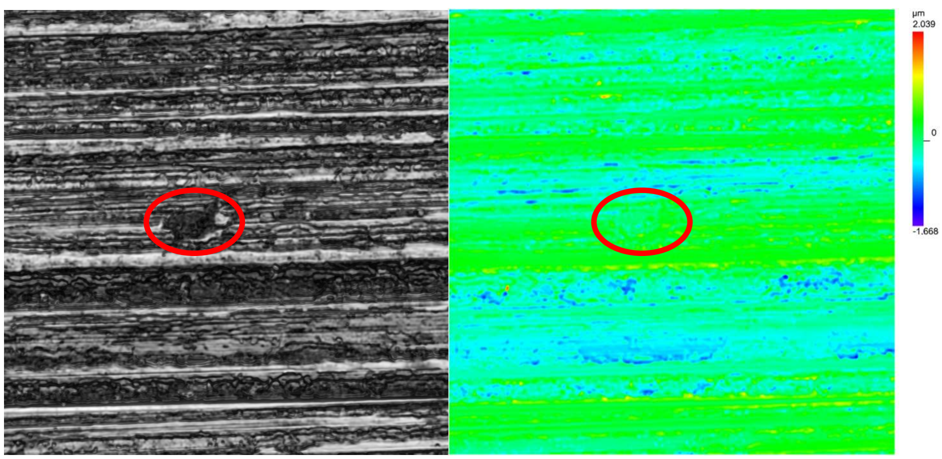

(a) (b)

Figure 4.4. Experiment 3: 5.5 V Roller Bearing Outer Race at 50X Lens, 4X Zoom in (a) grayscale/intensity image and (b) height profile image.

Experiment 3 underwent 34 nJ discharges but exhibited higher roughness coefficients than most of the 8100 nJ tests (no. 4, 7-8), which is likely due to both the shorter test duration and lower energy. Because the 90 V experiments ran for >50 days, the outer race of these tests were more worn down, especially with much higher energy discharges occurring, so it follows that the 5.5 V outer race exhibited high roughness coefficients with less wear. Note that the roughness coefficients of experiment 6 are comparable to experiment 3, but this may be due to the leftover oil that was hard to clean off the bearing race, since the other 90 V tests have lower roughness coefficients. Another interesting find from the 5.5 V test was the occurrence of huge defects seen at the 5X and 50X magnification lens. At 5X magnification, there were pits of ~5.1 µm with depths of ~46 µm while at 50X magnification, a few pillars had diameters ranging between 9.3-33.4 µm had heights of ~5.7 µm. These larger defects, being much bigger than the diameters of EDM damage found in [3] (~0.4 µm to ~1.8 µm), indicated some mechanical wear in the form of skidding and smearing caused by the light load on the roller bearing from the v-belt pulley system [15]-[17]. Although the 0 V mechanical test was conducted for a few days longer than the 5.5 V test, the 0 V bearing did not experience skidding/smearing. Therefore, it was concluded that the electrical discharges exacerbated the mechanical damage, as seen in the shorter 5.5 V test and also in the later 90 V experiments having increased skid/smear damage due to increased energies and longer test durations.

Experiments 4-8 were all 90 V, 8100 nJ experiments. Experiment 4 was the first pass comparison with the failed 90 V tests on ball bearings in [3]. The roller bearing in this first 90 V experiment already proved to be more robust than the ball bearing, which failed at 7.21 mm/s after 24.06 billion discharges [3] for the longest test duration of the three 90 V ball bearing experiments. The 90 V roller bearing was continuously run on the belted testbed under the same conditions past the 24.06 billion discharges after no indications of failure and did not fail even after 40.88 billion discharges. Because the highest failure threshold from the ball bearings was well surpassed, additional 90 V experiments were conducted to find the threshold of failure and to attempt to find a consistent pattern for the roller bearings. Figure 4.5 shows a sample cut from experiment 4, along with 3DLM images from the outer race. The red arrow indicates the “rollway” where the rollers passed over the outer race, and the images are taken from the worn path. There are visibly larger and more frequent defects from the 90 V experiment images compared to the 5.5 V (Fig. 4.3), but since the 90 V roller bearing did not fail, there is no visible fluting on any of the bearing components. The bigger “smudges” in the 3DLM images are the previously mentioned skid/smear damage where the melted steel was “smeared” under the roller onto the outer race. The diameters of these bigger defects range between 8.4 to 13 μm but they are shallow in height (~0.5 μm). The defects from skidding/smearing in this 90 V experiment averages smaller size parameters than that of the 5.5 V experiment, which can be attributed to the longer test duration and higher discharge energy causing the bigger defects to wear down over time. In higher resolution (50X lens, 4X zoom) image samples, the diameters of the pits/pillars were between 0.555 to 0.935 μm with heights/depths of 0.4 to 0.46 μm, and about 25 defects were seen in each sample.

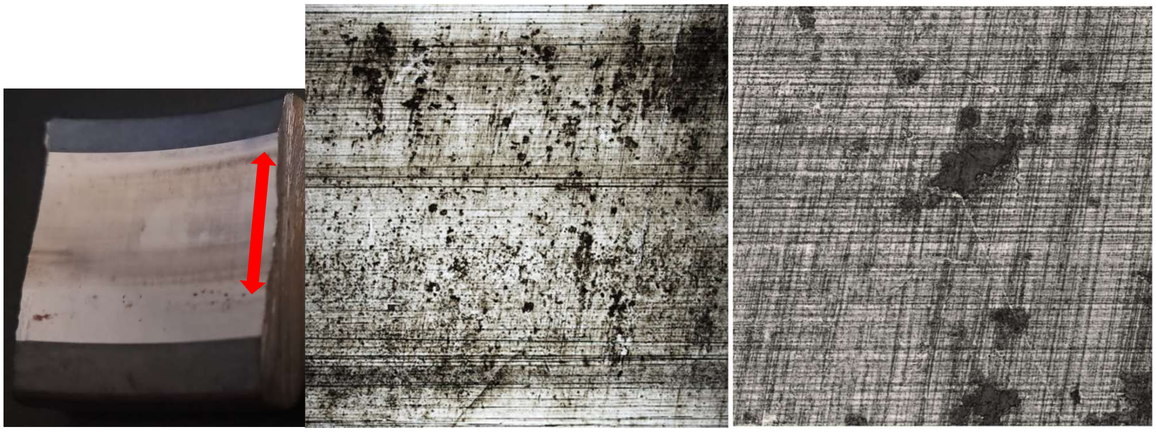

(a) (b) (c)

Figure 4.5. Experiment 4: 90 V Roller Bearing Outer Race (a) cut sample and imaged at (b) 5X Lens, 1X Zoom and (c) 50X Lens, 1X Zoom.

It is also important to note that the discharges in experiment 4 slowed down after 16.22 billion discharges for ~6 days, where 10 million discharges happened every few hours instead of the normal rate of 10 million every 7 minutes. It can be concluded that this change in rate of discharges was caused by the leakage of bearing oil since the cylindrical roller bearings used were open bearings. The discharges no longer had the same amount of oil to use as a path to shoot through the bearing; therefore, the rate of discharge slowed down tremendously. In the troubleshooting process, it was found that adding oil fixed the rate of the discharges. With this concept in mind, the results of experiment 5 were not analyzed due to its mechanical failure caused by lack of lubrication. Experiment 5 was still indispensable to this work because it revealed the need for occasional relubrication of the roller bearing. Because the oil film had thinned and ran out of the open bearing after 5 days of continuous operation, there was inadequate lubrication within the bearing, leading to increased friction and mechanical bearing failure at only 10.26 billion discharges. The rest of the experiments were closely monitored for adequate lubrication and re-oiled when needed so that mechanical wear would not be the reason for failure in these electrical discharge tests.

Experiment 6 was the first 90 V roller bearing test that failed, with the NDE ball bearing failing at the same time. The failures were indicated by the huge increase in audible noise on the testbed, where the metal scraping in the bearings was heard even with the rotor being spun by hand. As mentioned before, the Fluke meter did not detect failure. Figure 4.6 shows an image under 5X magnification, 1X zoom from the map of a sample from experiment 6 which clearly shows fluting. Of course, there were still larger defects of skidding/smearing present in this experiment, so the mechanical wear and electrical discharges were both mutually affecting each other and the damage on the bearing.

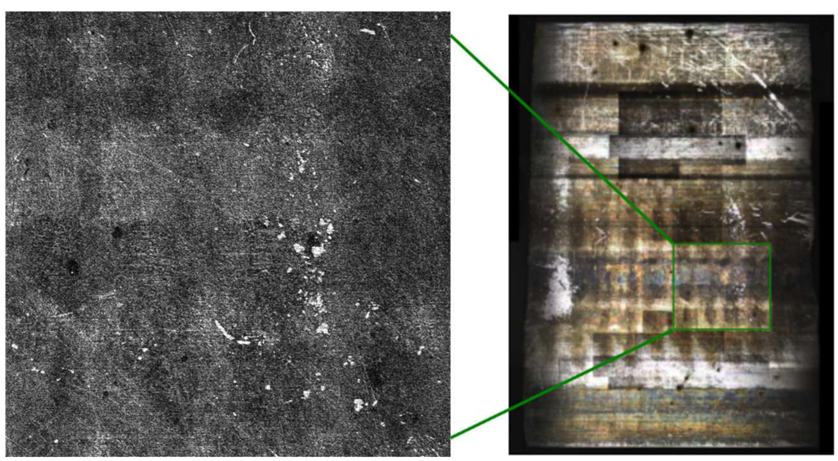

(a) (b)

Figure 4.6. Experiment 6: 90 V Fluted Roller Bearing Outer Race at (a) 5X Lens, 1X Zoom in (b) map of the sample.

Table 4.3 summarizes the average defect size parameters of the fluted 90 V experiments (no. 6-8) compared with the 0 V mechanical experiment (no. 2). Recall from Table 4.1 that experiment 7 exhibited the most EDM damage, with fluting on all components and failing at only ~50.09 billion discharges, while experiment 8 showed light fluting on the outer race, likely on the cusp on failure at the end of the experiment.

Table 4.3. Summary of Average Size Parameters for Roller Bearing Experiments under 50X Magnification Lens.

Experiment No.	1X Zoom Diameter [μm]	1X Zoom Height/Depth [μm]	4X Zoom Diameter [μm]	4X Zoom Height/Depth [μm]
2	1.4838	0.9512	0.9288	1.0496
6	89.066	0.6710	0.8316	0.7845
7	5.4273	2.8544	0.7030	0.7507
8	3.0903	0.8913	0.6630	0.7011

The 50X lens, 1X zoom results from the mechanical test are smaller in diameter than all the fluted 90 V tests, which is possibly due to the significantly shorter amount of time under test (1 week compared to more than a month). The bigger diameters from the 90 V tests are indication of skid/smudge marks, which was likely exacerbated by the energy discharges. The first fluted 90 V test had much larger diameters of smearing/skidding from the 50X magnification lens, 1X zoom images but had about the same size parameters when using the 4X zoom as the other fluted 90 V tests. Because the zoom causes a smaller area to image, it is hard to catch the bigger defects, though these smaller defects are probably nestled into the 1X zoom but are too small at that setting to detect using the software. Surprisingly, the defects for the mechanical test are only slightly bigger than the defects on the 90 V tests under the 4X zoom, but this could also be due to the test duration. The range in diameters are within the ones found for diameters of EDM [3], but the reported heights/depths of EDM in [12] are much larger than those found on the roller bearing races. These size characteristics will be further discussed later in this chapter.

Figure 4.7 shows the ultrasound data from experiment 7. The outliers indicate when the bearing was re-oiled, causing the ultrasound measurement to dip throughout the experiment. This test started at 45.5 dB and ended around 80.6 dB, where the line in the plot shows when the bearing reached the +35 dB threshold. The bearing at that time started getting audibly louder and may have been the first point of failure before the test was stopped for imaging. The trend looks like an exponential curve, but no curve-fitting method was applied to the data due to insufficient data sets (no repeatability) at this time for the ultrasound sensor. This is further confirmed by the lack of a trend for the ultrasound plot for experiment 8, which will be discussed following the 3DLM results for experiment 7.

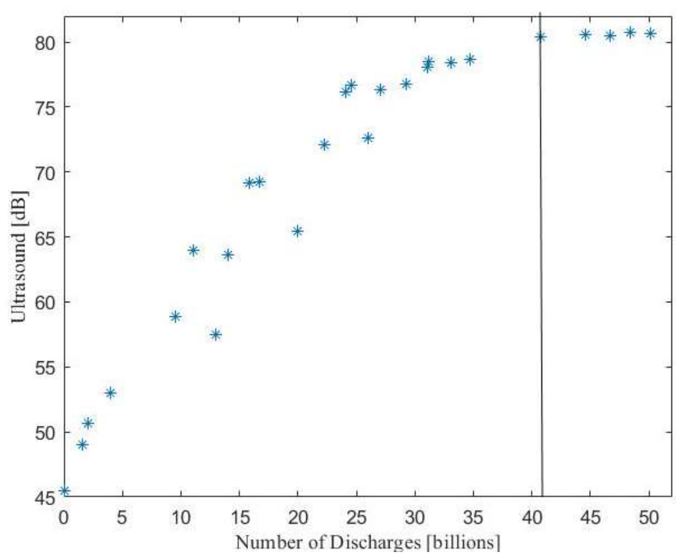

Figure 4.7. Experiment 7: Ultrasound Plot for 90 V Roller Bearing Test.

Figure 4.8 shows the fluted components of the bearing from experiment 7, and Figure 4.9 shows the 3DLM images taken from the outer race samples. It was surprising to see the higher frequency of the fluting from experiment 7 compared to experiment 6, appearing on a larger area of the outer race, and even appearing on all rollers and across the surface of the inner race. The intensity of EDM could have been affected by testbed misalignments, causing the bearing to fail at less than half the rate (~40 billion compared to 100 billion of experiment 6) due to those imbalances.

(a) (b) (c)

Figure 4.8. Experiment 7: 90 V Fluted Roller Bearing (a) Outer Race, (b) Inner Race, and (c) Roller (photos not to scale).

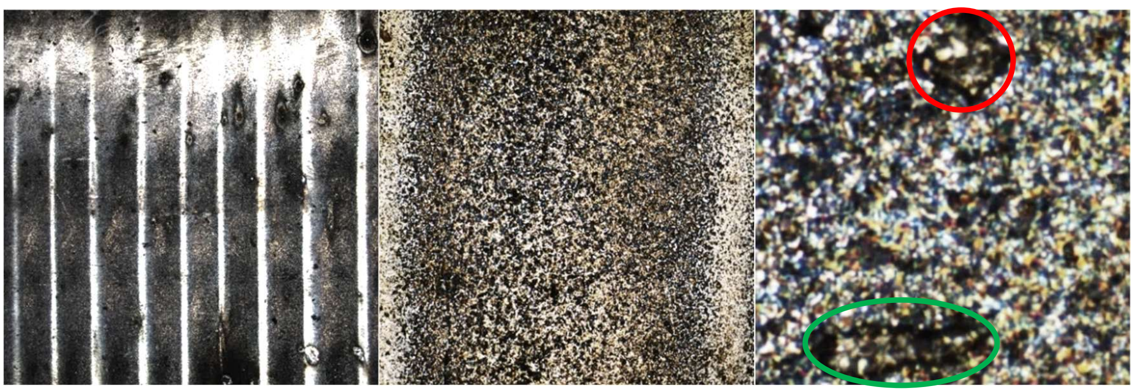

(a) (b) (c)

Figure 4.9. Experiment 7: 90 V Fluted Roller Bearing Outer Race at (a) 5X Lens, 1X Zoom, (b) 50X Lens, 1X Zoom, and (c) 50X Lens, 4X Zoom.

Figure 4.9(b) shows the center of a fluted line, and Fig 4.9(c) zooms into the pits and pillars as well as the "smudges" due to smearing. In Fig. 4.9(c), the top smear (red circle) was about 15 x 15 µm while the bottom one (green circle) was 27 x 10 µm in size. Again, further data must be taken and analyzed to study the effects that skidding of roller bearings have on EDM damage.

Figure 4.10 shows the clear fluting on both the rollers and the inner race, with defects being visible in lowest, 5X magnification lens. Figure 4.10(b) has dark sidebands due to the curvature of the roller, but the fluting is clearly seen down the middle of the image. The defects at 50X magnification, 1X zoom were unexpectedly smaller than those found on the outer race, with the roller defect diameter averaging 1.85 μm and heights/depths around 1.795 μm. This is likely due to smear/skid damage being more prevalent on the outer race and not the rollers, so it can be assumed that the roller defects were mainly caused by EDM. Meanwhile, the diameters for the inner race defects averaged 3.6 μm and 1.44 μm for the heights/depths. It follows that the inner race had larger defect diameters because of the small surface area, while the heights/depths of the defects were taller/deeper on the rollers because of the centrifugal forces that the rollers undergo when the bearing is spinning. The number of defects were more abundant on the rollers and inner race compared to the outer race, which was expected for the inner race since it is a smaller path/area for all the rollers to pass over. The cause for the rollers to have more defects than the outer race is due to the increased contact with their surfaces rolling on both the inner and outer race.

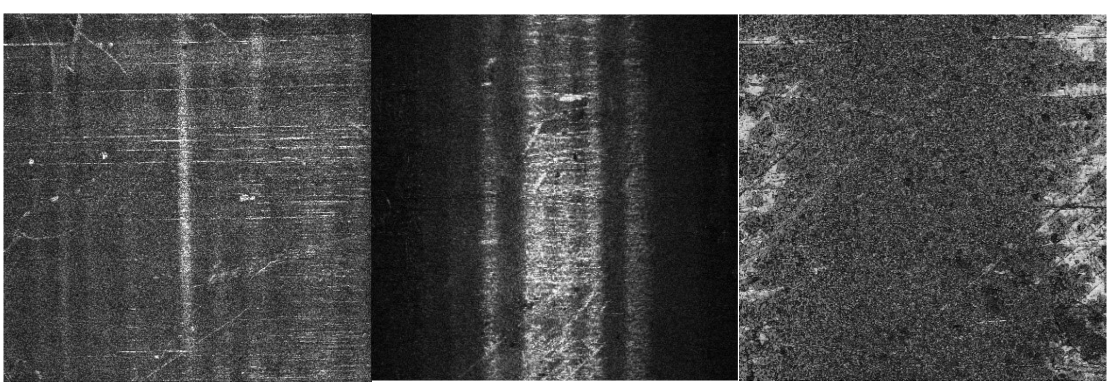

(a) (b) (c)

Figure 4.10. Experiment 7: 90 V Fluted Roller Bearing (a) Inner Race at 5X Lens, 1X Zoom, (b) Roller at 5X Lens, 1X Zoom, and (c) Roller at 50X Lens, 1X Zoom.

Figure 4.11 shows the ultrasound data from experiment 8. The outliers indicate when the bearing was re-oiled, causing the ultrasound measurement to dip throughout the experiment. The data points between 24 and 30 billion discharges were excluded due to inaccurately low measurements from the sensor. This test started at 49.4 dB and ended around 59.2 dB, not yet indicating bearing failure and only reaching the first alarm of Table 3.1 (increase of ~10 dB). Again, there is no clear trend in the data, so no curve fitting was attempted due to the uncertainty in the data set.

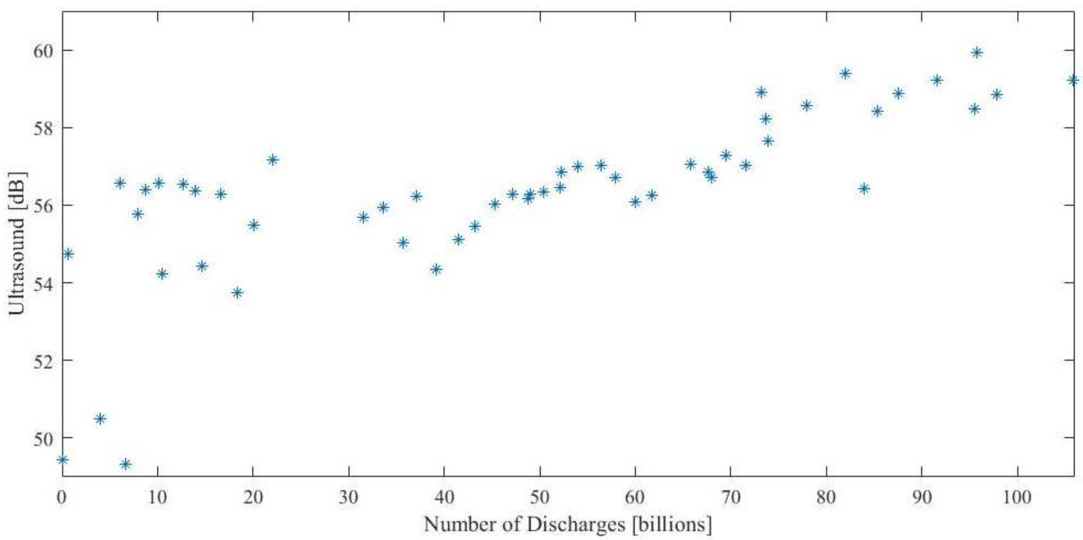

Figure 4.11. Experiment 8: Ultrasound Plot for 90 V Roller Bearing Test.

The increase in audible noise during the experiment was not noticeable, but there was light fluting on the outer race of this 90 V test after 105 billion discharges, so it could be assumed that the bearing was on the cusp of failure. However, the defect sizes, especially diameters, were considerably smaller than those seen in experiments 6 and 7, so the bearing seemed to have experienced less skid damage as well. Figure 4.12 shows the 3DLM images taken from the outer race sample, with purple arrows indicating the width of fluted lines. Most of the larger defects seen under the microscope were pits (Fig.

12(c) light blue and dark blue dots), which was interesting because the other 90 V tests saw a fairly even distribution of pits and pillars on the outer race.

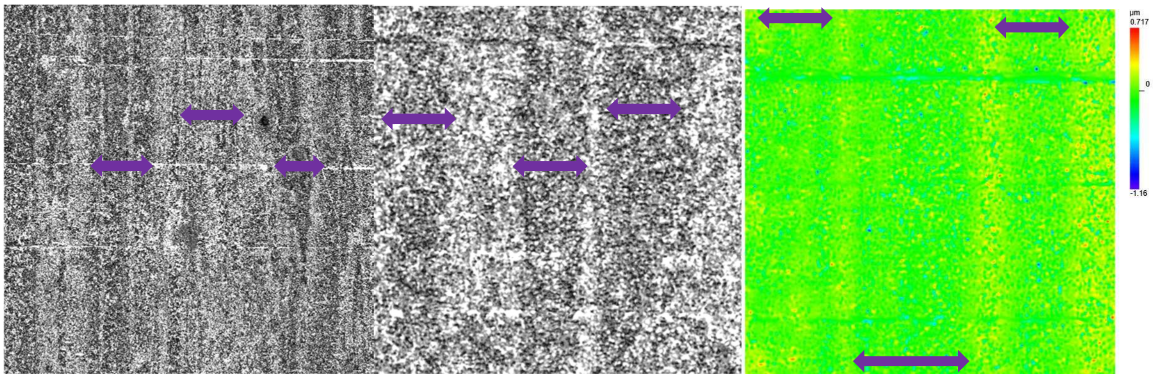

(a) (b) (c)

Figure 4.12. Experiment 8: 90 V Lightly Fluted Roller Bearing Outer Race (a) at 5X Lens, 1X Zoom, (b) 50X Lens, 4X Zoom, and (c) 50X Lens, 4X Zoom height profile.

With these inconsistent patterns between the experiments, some defects seen in the previous experiments could be due to mechanical wear, but the location of the images also play a factor in the size and characteristics of the defects. To further this point, the roughness of the 0 V roller bearing ranged between 0.62 and 0.76, depending on which part of the outer race, inner race, or roller was being sampled. Therefore, further analysis must be done before distinguishing the differences between mechanical and electrical wear and their interaction with each other.

Comparison with Ball Bearings and Journal Bearings

The roller bearing test results were compared with the ball bearing results of [3]. Figure 4.13 compares the 5.5 V test microscope images (all at default 1X zoom). EDM damage is clearly seen in the 5.5 V ball bearing samples (Fig. 4.13(a) & (b) bright spots) whereas it is not clear on the roller bearing samples. In higher magnification roller bearing images at 4X zoom, there were only about 8 pits and pillars found on the 4200 μm^2 image sample on the roller bearing while 20 defects appeared on an image sample of the same size from the ball bearing. The ball bearing defect diameters were between 0.262 to 0.836 μm, so it is fair to conclude that not all of the defects were caused by EDM, but only those >0.4 μm.

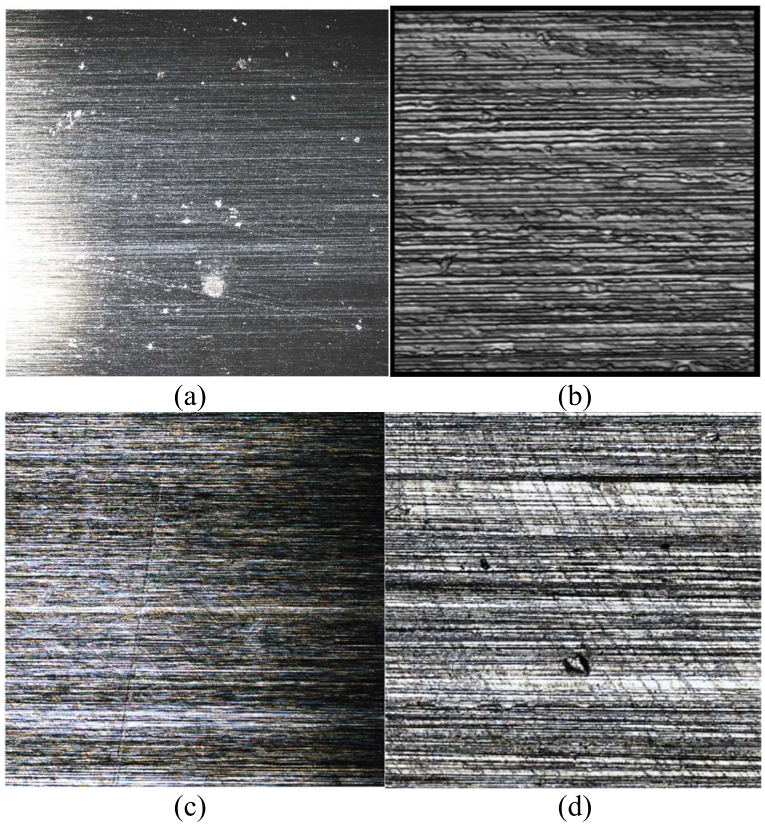

Figure 4.13. 5.5 V Bearing Test Comparison of (a) Ball at 5X Lens, (b) Ball at 50X Lens, (c) Roller at 5X Lens, and (d) Roller at 50X Lens.

Figure 4.14 compares the 90 V ball bearing results [3] with the fluted 90 V roller bearing of experiment 7 (zoom at default 1X unless otherwise specified). The large circular dark spots within the fluted lines of Fig. 4.14(c) were rust formed during the bearing cutting process, which was hard to remove before imaging. These spots were avoided when measuring roughness and defect sizes. Again, the larger spots under 50X magnification lens on Fig. 4.14(e) and (f) are indications of skid/smear damage (>3.678

μm diameters, >2.326 μm heights/depths). About 25 EDM defects were seen in each 4200 μm^2 fluted roller bearing sample, with diameters between 0.491-1.222 μm and depths/heights between 0.405-1.648 μm. Meanwhile, the 90 V ball bearing (top images) had about 60 defects per the same size samples that were ~1 μm in diameter and ≥1.25 μm tall/deep. The fluted roller bearing had a roughness coefficient of 0.7238 while the 90 V ball bearing had a roughness coefficient 0.8089 (average from image samples). The higher value for the ball bearing is not only due to the frosting of the bearing surface, but also because the surface curvature of the race affected the line profiles (tilt removal could not adjust for the entire curve).

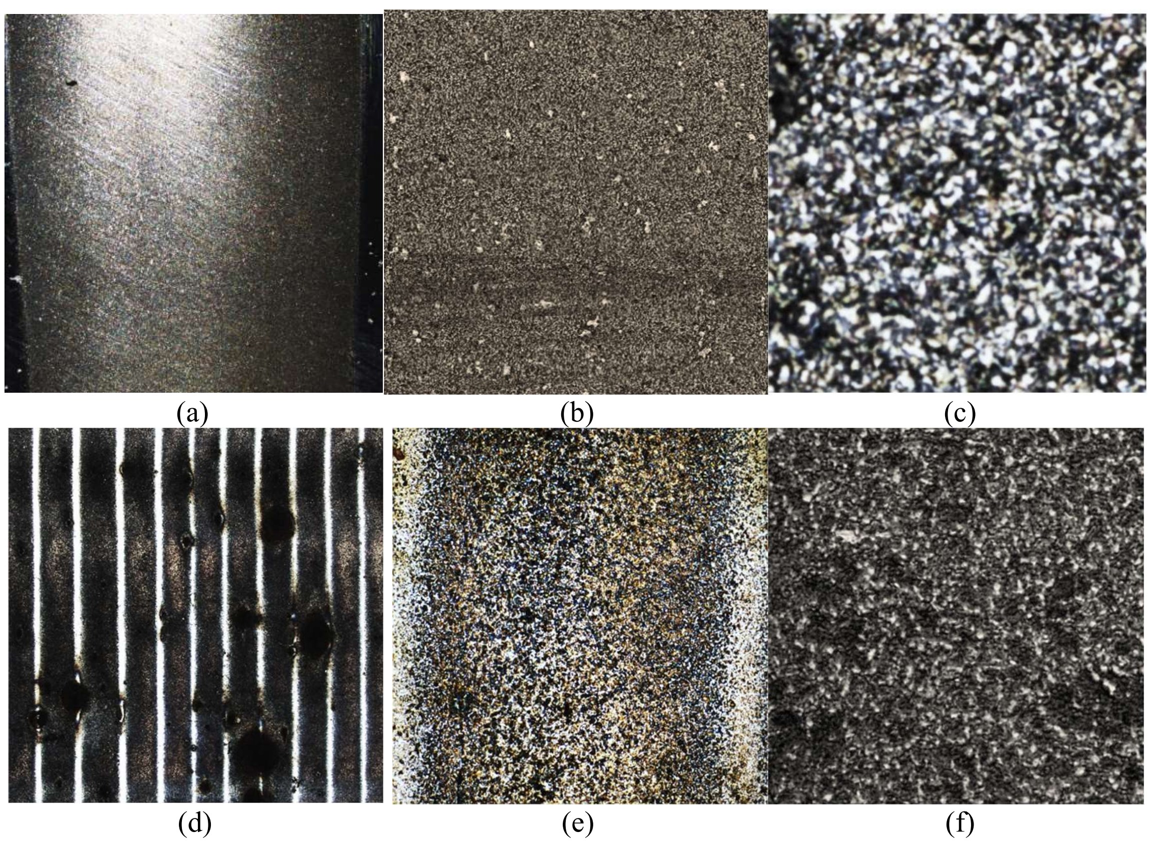

Figure 4.14. 90 V Bearing Test Comparison of (a) Ball at 5X Lens, (b) Ball at 50X Lens, (c) Ball at 50X Lens, 4X Zoom, (d) Roller at 5X Lens, (e) Roller at 50X Lens, and (f) Roller at 50X Lens, 4X Zoom.

While typical EDM damage has shown up as frosting on a ball bearing, longer areas of fluting were more prevalent on roller bearings, with shorter widths and often spanning ¾ of the length of the roller. This is due to the physical geometry of roller bearings, where there is a higher (~5X wider) contact surface area (indicated by red lines in Fig. 4.15). The rollers experience the discharges over a bigger surface, whereas the ball bearings have a smaller contact angle between the ball surface and the races, rendering a smaller path for discharges to shoot through. The frosted area of a 6306 ball bearing was found to be ~1.5 mm wide (Fig. 4.15(a) along the middle of the outer race), whereas the fluting found on the 90 V roller bearings were 3.5-9.5 mm wide. It was expected for the height/depths of EDM defects on the ball bearing to be taller/deeper than those found on the roller bearing. This is also supported by [12], where the average height/depths ranged between 0.9020 μm and 2.1358 μm. There are also more rollers (another factor for higher surface area) than balls in the same size bearings, which is why there was more damage on the rollers and inner race in the 90 V experiments.

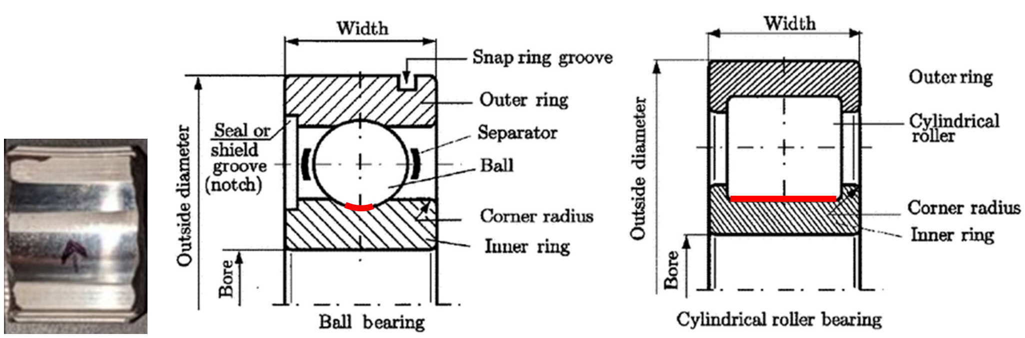

(a) (b) (c)

Figure 4.15. (a) Cut Ball Bearing Outer Race showing Frosting and Comparison of the Surface Contact Area of (b) 5 hp 6306 Ball Bearing vs. (c) Cylindrical Roller Bearing of the Same Size [30].

In addition to comparing the roller bearings with ball bearings, journal bearings were also tested under the 5.5 V, 34 nJ conditions until 6.138 billion discharges had occurred. A 0 V mechanical test was also conducted for about a week to compare between mechanical and electrical wear.

Again, as in the roller bearing experiments, the Fluke measurements did not increase, starting at 1.18 mm/s and ending on 1.56 mm/s for the mechanical test, and 0.79 mm/s (start) to 1.14 mm/s (end) for the 5.5 V test. Figure 4.16 shows the components of the ½” shaft diameter journal bearing used in testing. Only the images of the bottom of the split housing are presented due to microscope stage and working distance constraints. The oil during the tests often turned black during bearing operation, likely due to housing surface contaminants and exacerbated by energy discharges. The shaft brush marking indicates where the discharges were applied. Interestingly, throughout the entire 5.5 V experiment, the discharges would sometimes not fully break down, which had to be troubleshooted to ensure the most accurate discharge count, because the Arduino was not programed to decipher between full and partial discharges of the capacitors used. Figure 4.17 shows an oscilloscope capture of the discharges that did not fully break down.

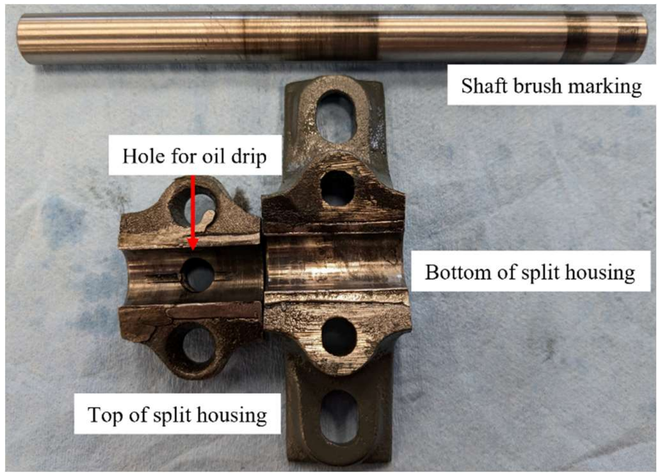

Figure 4.16. Journal Bearing Components with ½” Diameter Shaft.

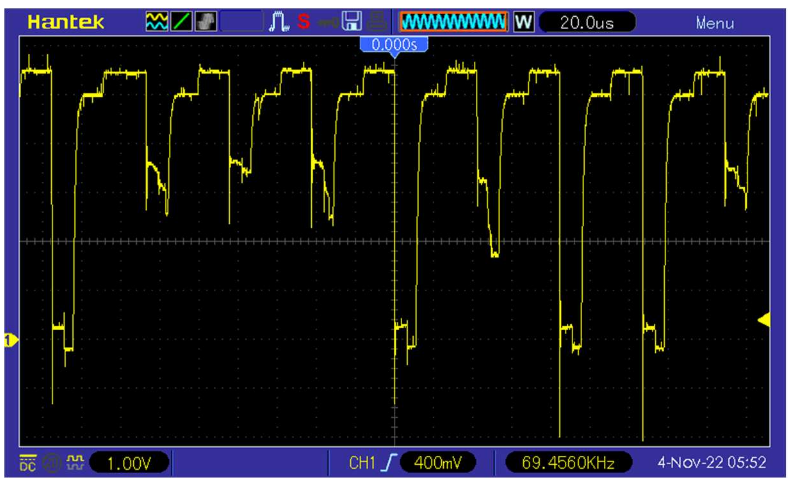

Figure 4.17. Journal Bearing 5.5 V Discharge Profile.

As shown in Fig. 4.17, the discharges would sometimes only discharge halfway before the capacitors were charged to full again. The discharge circuitry was investigated, and several components such as resistors were swapped out to adjust the time constant and cause the discharges to fully break down before the capacitor was charged again. These did not affect the partial break down behavior, and it was found that letting the oil drip at an adequate pace would help the discharges fully go through the bearing, similar to the findings of roller bearing experiment 5. Further research must be done to characterize this relationship between oil film thickness and electrical discharge behavior, especially considering the different properties of a journal bearing such as oil whirl or eccentricity [20] but this was outside the scope of this thesis. With the constant irregular behavior of the discharges, the test was often paused to ensure that the discharges were fully breaking down, causing the test to take longer to reach the 6.1 billion discharge threshold for comparison with the 5.5 V ball and roller bearing experiments. The “step” ridges on the top of the discharge curve were disregarded because it was a confirmed behavior of the journal bearing discharges after using a different oscilloscope to monitor the discharges. These ridges could be due to the shaft brush having two carbon brushes instead of one or due to the oil film within the bearing itself causing distortion to the discharge profile.

Table 4.4 shows the 3DLM results of the journal bearing experiments. A default of 1X zoom was used for both 5X and 50X magnification settings. The roughness coefficients were similar overall, which was expected due to the low energy discharge and similar test duration times. The large defects for both tests were likely due to babbitt fatigue, although it was expected that the energy discharges of the 5.5 V experiment would cause different defect behavior and sizes. The EDM discharges may have played a role in the depths of the 5X magnification samples, causing the defects to be ~25 μm taller/deeper (on average) than those of the 0 V mechanical test. However, it is hard to tell without more experimental results if the electrical wear truly affects the mechanical wear, and to what extent. Furthermore, the diameters under 50X magnification were almost 4X greater in the mechanical test than those of the 5.5 V experiment, which confirms the need for future work in characterizing EDM in journal bearings.

Table 4.4. Summary of 3DLM Results for Journal Bearing Experiments.

3DLM Parameter	0 V Mechanical Test	5.5 V Test
Overall Roughness Coefficient	0.8129	0.8107
5X Lens Roughness Coefficient	0.8491	0.8595
50X Lens Roughness Coefficient	0.7679	0.7816
5X Lens Diameter [µm]	3.8747	2.9344
5X Lens Height/Depth [µm]	74.5922	99.7547
50X Lens Diameter [µm]	23.5672	8.4875
50X Lens Height/Depth [µm]	3.9529	4.0221

Figure 4.18 shows the 3DLM images from the journal bearing experiments. Again, a default of 1X zoom was used for both 5X and 50X magnification. The red arrows indicate the direction of the shaft length. The images are all similar in showing babbitt fatigue spots in brighter and darker areas for both experiments. There are smaller damage spots for the 5.5 V experiment under 50X magnification in Fig. 4.18(d), illustrating the average defect sizes being smaller as in Table 4.4.

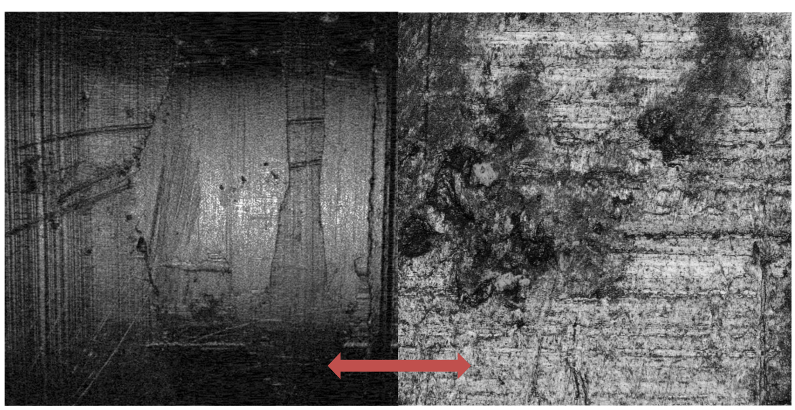

(a) (b)

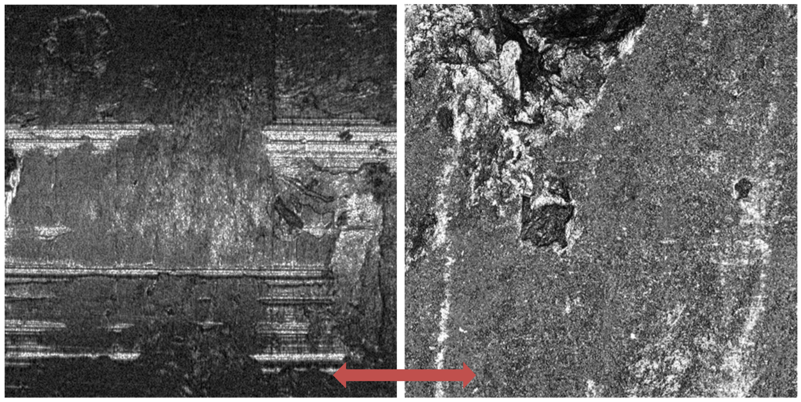

(c) (d)

Figure 4.18. Journal Bearing Test Comparison at (a) 0 V under 5X Lens, (b) 0 V under 50X Lens, (c) 5.5 V under 5X Lens, and (d) 5.5 V under 50X Lens.

Under 5X magnification, it looks like the polish lines of the 5.5 V test are perpendicular to the ones on the mechanical test housing, but this change in direction was due to the wear from the shaft at different locations of the housing. The polish lines seem to “change” on the surface of the same housing because of the slight loading in the coupled system and inconsistent spinning behavior of the shaft. probably due to less surface area than ball/roller bearings. Comparing the journal bearing results to the 5.5 V ball and roller bearing experiments, the defects are definitely larger (by 4X) but also less frequent under the 5X and 50X magnification at 1X zoom. However, at 50X lens, 4X zoom, pits and pillars were found with diameters between 0.415-1.662 µm and heights/depths between 0.560-1.284 µm. These defect sizes were similar to 5.5 V ball bearing findings in [3] and EDM damage heights/depths in [12], so they could be characterized as EDM damage, but more experimental results under different discharge energies should be obtained before coming to this conclusion. Future work should try to use journal bearings with about the same surface area as the ball bearings for a better comparison as well.

Discussion and Lifetime Prediction of Cylindrical Roller Bearings

The main focus of the presented research was on the cylindrical roller bearings in order to provide groundwork for higher power bearings in VFD applications, especially with WBG devices, and to explore EDM damage thresholds for those applications. Because of the inconsistency in number of discharges to failure for the accelerated 90 V roller bearing experiments, the following lifetime prediction is conceptual and should be further researched. Taking the average of the number of discharges to failure of roller bearing experiments 6-8 to be ~85.51 billion discharges, it can be concluded that the roller bearings last ~3.55 times longer than a ball bearing (based on the highest number of discharges to failure of the 90 V ball bearing tests of 24.06 billion discharges [3]). The number of discharges to failure for the other accelerated ball bearing experiments of [3] (discharge energies of 4900 nJ and 6400 nJ) were then multiplied by 3.55 to extrapolate backwards and show the lifetime prediction of the roller bearings.

Figure 4.19 shows the conceptual lifetime prediction of roller bearings, with the asterisks at 8100 nJ being the results from roller bearing experiment 6-8, the asterisks at 4900 nJ and 6400 nJ being the estimated failures using the ball bearing experiments 2-3 of Table 6.3 in [3] as the baseline, and the orange line being the linear curve fit generated by MATLAB based on those 5 data points. The gray box highlights the region of motor operation [3]. The slope of the line (*m*) was -77.06 with the y-intercept (*b*) at 713.8, and the calculated R^2 value was 0.9459, revealing that this linear fit represents the data well. Confidence intervals were not calculated because this is just a conceptual comparison with the lifetime of ball bearings presented in [3] and [12]. It is important to note that the x-intercept of ~9263 nJ is greater than the 9000 nJ presented in [3], which was expected since the cylindrical roller bearings proved to be more robust than ball bearings due to their increased surface area as discussed earlier in this chapter.

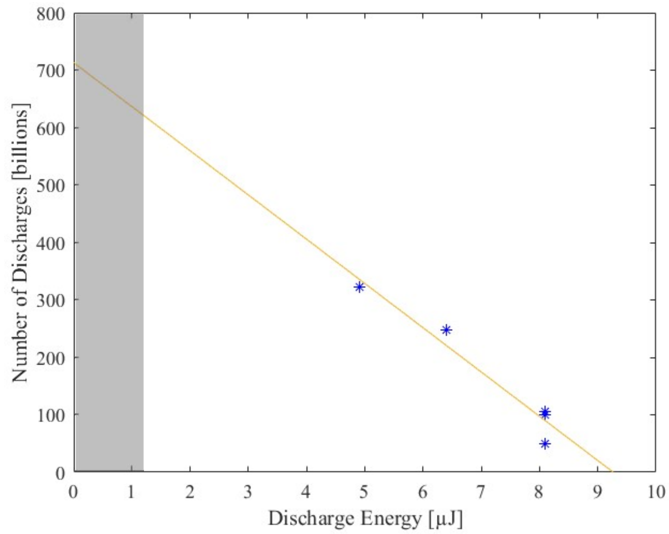

Figure 4.19 Preliminary Lifetime Prediction Model for Cylindrical Roller Bearings.

From the orange fit line in Fig.4.18, it can be assumed that the cylindrical roller bearing will endure more than ~3.5 times more discharges than a ball bearing before failure (*b*=201.8 billion for the curve fit from [3]), which was the same hypothesis used to form the conceptual lifetime prediction. However, this plot is preliminary because no further research has been done on the oil properties during energy discharges in roller bearings, and therefore cannot be compared with the work in [3] that explains the expectation for the line to be curved rather than linear in real motor operations which thin the grease over time.

Furthermore, the results presented are solely based on the DE roller bearing, but future work must be done to explore the behaviors of a cylindrical roller bearing in motor operations, especially since the NDE bearing will likely be a ball bearing that may or may not be insulated. A brief investigation of what the NDE bearing was experiencing was conducted for the SKF ball bearing that was used in roller bearing experiments 4-6. A probe was used to read 60-65 V peak-to-peak shaft voltage, which was much higher than expected and revealed that discharges were traveling down the shaft from the DE. The NDE vibration was measured to be ~2.88 mm/s after 151.75 billion discharges (65 V NDE shaft voltage, 520 nJ based on 246 pF bearing capacitance [3]) to have a comparison between the DE roller bearing and the NDE ball bearing. The Fluke vibration did not indicate failure, but as mentioned before, the bearing was considered failed when metallic scraping was heard when turning the rotor by hand. With more research on NDE bearing behavior, a ratio could be found for the failure rate of each rotor end compared to the number of discharges, which could lead to significant lifetime assessment of both bearings in WBG high dv/dt applications.

An attempt to create a finite element model (FEM) of the roller bearing under energy discharges was also pursued during the experiments. The bearing capacitance was measured using methods from [3] and [12], but upon entering the measured values into a PSpice circuit optimizer, the software did not converge to a single bearing capacitance value. Several discharge profiles of different energies were used, yet the PSpice LSQ optimizer was unable to get under 20% error for the bearing capacitance and resistance. Therefore, future work needs to be done on finding an acceptable value for the bearing capacitance in order to create an accurate FEM of cylindrical roller bearings experiencing energy discharges.

CHAPTER FIVE

Conclusions and Future Work

The research presented in this thesis provides valuable groundwork in advancing from lower power ball bearings to higher power motor drive applications focusing on the damage characteristics of higher power roller and journal bearing applications using accelerated aging tests. Findings show less EDM damage on the roller bearing surfaces for the same amount of discharges, potentially due to the fact that the ball bearing contact area is much smaller (more concentrated) than the cylindrical roller bearing. EDM damage in the form of fluting rather than frosting was found in failed roller bearing experiments. It was also concluded that the oil film thickness greatly affects the energy discharge behavior within both the roller and journal bearings. Nonintrusive bearing monitoring methods were explored, including ultrasound detection, and roughness coefficients and defect size parameters were also compared between ball, roller, and journal bearings.

Further work must be done to differentiate mechanical wear vs. electrical damage, and to analyze their effects on one another. The initial research to advance the bearing current research from ball bearings to larger roller and journal bearings has yielded strong comparisons to the ball bearings where the next steps in future work could include:

- Studying the effects of oil film thickness under electrical discharges.
- Implementing larger discharge energies in journal bearing testing.
- Applying load/temperature to the accelerated lifetime belted testbed.

- Comparing roller bearing results on the unmodified and modified IM.
- Adding conductivity to oil to try to mitigate EDM damage as in the ball bearings.

These studies will also help in finite element analysis (FEA) of what is happening within the roller and journal bearings, which can then be scaled to higher power systems. Ultimately, this research will answer questions about electric propulsion in a variety of transportation and even within the power generation sector.

APPENDIX

APPENDIX

MATLAB Scripts to Obtain the Ultrasound Sensor Signal

This script was based off the work in [3] in collecting piezo sensor data and modified such that the ultrasound raw voltage signal would be acquired, recorded to a spreadsheet, then run through the transfer function given by [11] to plot real time data as an experiment was running on the belted testbed. Note that the base dB was calculated from a manual calculation of the first set of data collected at the start of the experiment.

```
% Hellen Chen (adapted from Ryan Collin's vibration_experiment.m)
% Baylor Energy and Renewable Systems Lab
% This script executes the bearing ultrasound vibration measurements

% Before starting script, make sure k is at the proper index by
creating
% variable in the workspace first

ultrasound_data = zeros(50,1000);

base_dB = 47.8731; % UT850S reading from Sep 16, 2022 AM
plot(0,base_dB,'*')
hold on

while(1)

    ultrasound_data(k,(1:1000)) = get850Data();
    xlFilename = 'C:\Users\hellen_chen\Documents\Bearing
Testbed\bearing89.xlsx'; % create a directory
    xlRange = strcat('U',int2str(k));
    xlswrite(xlFilename,ultrasound_data(k,:),'ultrasound',xlRange);

    t = datestr(datetime('now'))
    xlRange = strcat('A',int2str(k));
    xlswrite(xlFilename,t,'ultrasound',xlRange);

    current = mean(ultrasound_data(k,(1:1000))) /200 * 1000; %
(2V/div), 200 Ohm resistor, A to mA
    dB = 6.3211 * current - 2.9169; % UT850S transfer function
    plot(k,dB,'*')
```

```
    if (dB - base_dB) > 35
        disp('catastrophic bearing failure impending: PLEASE STOP
TEST')
    elseif (dB - base_dB) >16
        disp('warning: may be starting to fail')
    elseif (dB - base_dB) > 8
        disp('warning: may need oil')
    else
        % do nothing
    end

    fprintf('k = %d\n', k);
    k = k+1;

    pause(21600) % collect data every 6 hours

end
```

The function `get850Data()` within the script above was used to acquire and transfer voltage probe data from a Tektronix MDO3014 oscilloscope to a connected PC. It is shown below and was also modified from MATLAB code used in [3], with main changes to the parameters section.

```
function [v] = get850Data()

% notes about code operation
% commands modify oscilloscope settings or tell the scope to perform a
% specific action
% queries cause the scope to return data and status information

% most commands have a set form and a query form. the query form of the
% command has a question mark at the end. some commands have set only
and
% some have query only

% Parameters to set          % based on the update time of the sensor
horizscale = 40;             % 40s/div; 2.5S/s aka 2.5Hz sampling freq
record = 1000;               % 1000 data points (lowest setting)

% CH2 settings
CH1_v_div = 2;           % CH1 V/div;
CH1_pos = 0;             % CH1 position
trig_level = 0;          % trigger position

% user inputs
visa_vendor = 'tek';
visa_addr = 'USB0::0x0699::0x0408::B021904::INSTR';
```

```
% instrument connection config
% if ~isempty(instrfindall)
%     fclose(instrfindall);
%     delete(instrfindall);
% end

scope = visa(visa_vendor, visa_addr); % create the scope object
scope.InputBufferSize = 10e3;   % total size of the input buffer, must
be >= size of vector to be collected
fopen(scope); % connects the object scope to the instrument

fprintf(scope, '*cls'); % clears the scope (ESR)
ID = query(scope, '*idn?'); % request and store the scope ID
fprintf('Connected to: %s', ID);

fprintf(scope, '*rst'); % reset scope
query(scope, '*opc?'); % synchronize the operation of the scope with
application program. Returns 1 when all commands are complete

% set up the horizontal time/div and record length
fprintf(scope, 'horizontal:scale %d', horizscale); % set the horizontal
scale of the scope
fprintf(scope, 'horizontal:recordlength %d', record); % set the record
length

% set up Channel 1
fprintf(scope, 'CH1:scale %d', CH1_v_div); % set the CH1 volts/div
fprintf(scope, 'CH1:position %d', CH1_pos); % specifies the channel
offset
fprintf(scope, 'fpanel:turn triglevel, %d', trig_level);

%%%%%%%%%%%%%%%%%%%%%%%%%%%%%%%%%%%%%%%%%%%%%%%%%%%%%%%%%%%%%%%%%%%%%%%%%
%%%%
% io config, configure the scope setting, set up to collect from CH2

fprintf(scope, 'data:source CH1'); % channel selection

fprintf(scope, 'header 0'); % turns off the header
fprintf(scope, 'data:encdg SRIBINARY'); % specifies the encoding format
for outgoing waveform data (in this case signed integer)
fprintf(scope, 'data:start 1'); % first sample
fprintf(scope, 'data:stop %d', record); % last sample
fprintf(scope, 'wfmoutpre:byt_nr 1'); % 1 byte per sample

% acq config
fprintf(scope, 'acquire:state 0'); % stop, make sure it is off
fprintf(scope, 'acquire:stopafter SEQUENCE'); % single sequence
acquisition mode
fprintf(scope, 'acquire:state 1'); % acquire aquisition on screen
query(scope, '*opc?'); % allow things to sync

% retrieve scaling factors
vscale = str2double(query(scope, 'wfmoutpre:ymult?')); % volts / level
```

```
voff = str2double(query(scope, 'wfmoutpre:yoff?')); % vertical position
of the source waveform in digitizing units (digitizing levels per
vertical division)

% get waveform data
pause(400)
fprintf(scope, 'curve?'); % transfers data from the oscilloscope
v = (vscale * (binblockread(scope, 'int8') - voff))'; % with 8 bit
precision

% error checking
r = query(scope, '*esr?'); % returns the contents of the standard event
status register
%fprintf('event status register: 0b%x\n', r);
r = query(scope, 'allev?'); % prompts the scope to return all events
and their messages
%fprintf('all event messages: 0b%x\n', r);

% CH1 collection complete
%%%%%%%%%%%%%%%%%%%%%%%%%%%%%%%%%%%%%%%%%%%%%%%%%%%%%%%%%%%%%%%%%%%%%%%
%%%%

% gracefully close visa session
fclose(scope);
delete(scope);
clear scope;

end
```

BIBLIOGRAPHY

[1] A. von Jouanne and A. Yokochi, “A Short Course on Variable Frequency Drive Application Issues”, Baylor University, Waco, Mar. 2019.

[2] A. von Jouanne *et al*., "Motor Bearing Current Characterization in SiC- based Variable Frequency Drive Applications," *2020 IEEE Energy Conversion Congress and Exposition (ECCE)*, Detroit, MI, USA, 2020, pp. 2718-2725, doi: 10.1109/ECCE44975.2020.9235925.

[3] R. Collin, “The Impact of Conventional and Wide Bandgap Semiconductor PWM Inverter EDM Bearing Currents on Motor Bearings,” Ph.D. dissertation, ECE, Baylor Univ., Waco, TX, 2022.

[4] R. Collin, M. Stephens and A. von Jouanne, "Development of SiC-Based Motor Drive Using Typhoon HIL 402 as System-Level Controller," *2020 IEEE Energy Conversion Congress and Exposition (ECCE)*, Detroit, MI, USA, 2020, pp. 2689-2695, doi: 10.1109/ECCE44975.2020.9236201.

[5] O. Magdun, Y. Gemeinder, and A. Binder, "Investigation of influence of bearing load and bearing temperature on EDM bearing currents," *2010 IEEE Energy Conversion Congress and Exposition*, Atlanta, GA, USA, 2010, pp. 2733-2738, doi: 10.1109/ECCE.2010.5618061.

[6] A. Joshi, “Electrical Characterisation of Bearing Lubricants.” *Karakterisering Och Modellering Av Lagerströmaktivitet*, 2019.

[7] P. Zhang, Y. Du, T. G. Habetler, and B. Lu, “A survey of condition monitoring and protection methods for medium-voltage induction motors,” *IEEE Transactions on Industry Applications*, vol. 47, no. 1, pp. 34-46, Jan.-Feb. 2011.

[8] ISO 13373-1:2002(en): Condition monitoring and diagnostics of machines — Vibration condition monitoring — Part 1: General procedures.

[9] Z. Taha and I. Pranoto, “Acoustic Emission Application for Monitoring Bearing Defects,” Acoustic Emission - Research and Applications, Mar. 2013, doi: 10.5772/55434.

[10] A. Ahmed, A. Istiak, and M. M. Helali. (2020). Vibration Analysis of Rolling Element Bearing using Micro Electro-Mechanical System (MEMS) Based Accelerometer. Presented at ICMIEE. [Online]. Available: https://www.kuet.ac.bd/icmiee2020/Technical_and_Keynote_papers/All_Paper/ICMIEE20-084.pdf.

[11] J. Jung *et al*., "Monitoring Journal-Bearing Faults: Making Use of Motor Current Signature Analysis for Induction Motors," in *IEEE Industry Applications Magazine*, vol. 23, no. 4, pp. 12-21, July-Aug. 2017, doi: 10.1109/MIAS.2016.2600725.

[12] M. Stephens, “Wide Bandgap Inverter Duty Bearings: Development and Lifetime Prediction of Conductive Grease Bearings with Integrated Graphene Nanoparticles.” to be published, Ph.D. dissertation, ECE, Baylor Univ., Waco, TX, 2025.

[13] S. Mitra and C. Koley, "Different measurement techniques for detection of bearing faults in industrial actuators — comparative study," *2017 IEEE Calcutta Conference (CALCON)*, Kolkata, India, 2017, pp. 412-417, doi: 10.1109/CALCON.2017.8280766.

[14] G. Singh, T. C. A. Kumar, and V. N. A. Naikan, "A non intrusive methodology for bearing current detection in PWM inverter fed induction motor drive," *2018 International Conference on Power, Instrumentation, Control and Computing (PICC)*, Thrissur, India, 2018, pp. 1-6, doi: 10.1109/PICC.2018.8384807.

[15] R.S. Dwyer-Joyce, P. Harper, and B. Drinkwater, “A Method for the Measurement of Hydrodynamic Oil Films Using Ultrasonic Reflection,” *Tribology Letters 17*, 2004, pp. 337–348, https://doi.org/10.1023/B:TRIL.0000032472.64419.1f

[16] M. Li, M. Jing, Z. Chen, and H. Liu, “An improved ultrasonic method for lubricant-film thickness measurement in cylindrical roller bearings under light radial load,” *Tribology International*, Volume 78, 2014, Pages 35-40, ISSN 0301-679X, https://doi.org/10.1016/j.triboint.2014.04.023.

[17] “UltraTrak 850S Smart Analog Sensor,” ed: UE systems, 2021.

[18] F. He, G. Xie, and J. Luo, “Electrical bearing failures in electric vehicles,” *Friction Tsinghua Journals*, vol. 8, no. 1, pp. *4–28*, Dec, 2019. Accessed on: Jan, 23, 2023, doi.org/10.1007/s40544-019-0356-5, [Online].

[19] A. Gonda, R. Capan, D. Bechev, and B. Sauer, “The Influence of Lubricant Conductivity on Bearing Currents in the Case of Rolling Bearing Greases,” *Lubricants*, vol. 7, no. 12, p. 108, Dec. 2019, doi: 10.3390/lubricants7120108.

[20] NSK, Japan. *Rolling Bearings*. (2013). Accessed: Aug. 1, 2022. [Online]. Available: https://www.nsk.com/common/data/ctrgPdf/bearings/e1102m.pdf

[21] Z. Yu and Z. Yang, "Fatigue Failure Analysis of a Grease-Lubricated Roller Bearing from an Electric Motor," *Journal of Failure Analysis and Prevention,* vol. 11, *(2)*, pp. 158-166, 2011. Available: doi:10.1007/s11668-010-9422-z

[22] Q. Zhang, J. Luo, X. Xie, J. Xu, and Z. Ye, "Experimental Study on the Skidding Damage of a Cylindrical Roller Bearing," *Materials*, vol. 13, no. 18, p. 4075, Sep. 2020, doi: 10.3390/ma13184075.

[23] A. Kumar. "Journal Bearing – Types, Lubrication, Uses, Diagrams." Marinerspoint Pro. https://marinerspointpro.com/journal-bearing-types-uses-materials/ (accessed Aug. 15, 2022).

[24] U. Werner, "Vibrations caused by noncircular shaft journals – a mathematical model for rotordynamic analysis of electrical motors with sleeve bearings," *Journal of Mechanical Science and Technology*, vol. 27, *(2)*, pp. 337-351, 2013. Available: doi:10.1007/s12206-012-1250-5

[25] M. E. Leader, "Understanding Journal Bearings," Applied Machinery Dynamics Co., Durango, Colorado, USA, Date. Accessed: Sep. 23, 2022. [Online]. Available: http://edge.rit.edu/edge/P14453/public/Research/2-_LEADER_-_Understanding_Journal_Bearings.pdf.

[26] A. von Jouanne *et al*., "Development of Inverter Duty Motor Bearings for Si and SiC-Based Variable Frequency Drive Applications Including Advanced 4D Finite Element Modeling," *2021 IEEE Energy Conversion Congress and Exposition (ECCE)*, Vancouver, BC, Canada, 2021, pp. 5154-5161, doi: 10.1109/ECCE47101.2021.9595862.

[27] BESTORQ., Lincoln NE, USA. *V-Belt Installation, Maintenance & Storage*. Accessed: Mar. 2, 2022. [Online]. Available: https://www.bestorq.com/Library/TechInfo/techinfo/V-Belt%20Installation-Maintenance-Storage.pdf.

[28] OLYMPUS., Tokyo, Japan. *Introduction to Surface Roughness Measurement: Roughness Measurement Guidebook*, (2021). Accessed: Feb. 2, 2023. [Online]. Available: https://www.olympus-ims.com/en/metrology/surface-roughness-measurement-portal/parameters/.

[29] "Belt drive motors." SKF.com. https://www.skf.com/us/industries/general-machinery/electric-motors/electric-motors-and-generators/belt-drive-motors (accessed Mar. 9, 2023).

[30] D. B. Marghitu, C. I. Diaconescu, and N. Craciunoiu, "Machine Components," in *Mechanical Engineer's Handbook*. USA: Elsevier, 2001, ch. 5, sec. 4, pp. 299. [Online]. Available: https://app.knovel.com/hotlink/pdf/id:kt00C5H7A2/mechanical-engineers/geometry.